國立交通大學

電機資訊學院

光電工程研究所

碩士論文

探討掃描光學顯微術之一些新功能

Exploring New Functionalities of Scanning Optical Microscopy

研究生：王雲漢

指導教授：黃中垚 教授

中華民國九十七年二月

探討掃描光學顯微術之一些新功能

Exploring New Functionalities of Scanning Optical Microscopy

研究生：王雲漢　　Student：Yuen-Han Wang

指導教授：黃中垚　　Advisors：Professor Jung Y. Huang

國立交通大學電機資訊學院

光電工程研究所

碩士論文

A Thesis Submitted to
Department of Photonics and Institute of Electro-optical Engineering
College of Electrical Engineer and Computer Science
National Chiao Tung University
in Partitial Fulfillment of the Requirements
for the Degree of
Master
in
Electro-optical Engineering

February 2008
Hsinchu, Taiwan, Republic of China

中華民國九十七年二月

探討掃描光學顯微術之一些新功能

研究生：王雲漢　　指導教授：黃中垚 教授

國立交通大學

光電工程研究所

摘要

本論文的第一個部份是呈現出利用單光子鎖模偵測技術來分析表面穩定鐵電液晶的動態調制，此技術不但可以有效的抑制拉曼光譜的直流基底，而且會產生有關特定之拉曼最高點的振幅及相位調制。摻雜氧化鋅奈米微粒會比未摻雜的表面穩定鐵電液晶以比較有組織性的狀態隨外加調制電場轉動，並且因此對於高頻率轉動所產生的混亂效應會有較好的抗性。此方法提供傳統的拉曼顯微術新的功用，對於探討在薄膜中具有電光主動性之空間分佈及動態調制。

在第二部份我們會藉由表面增強拉曼散射的技術來調查由於奈米柱的高外觀比例所造成的拉曼散射光譜的方位角相依性以及利用單光子鎖模偵測技術測量 8CB 分子吸附在銀奈米柱陣列上的拉曼圖像。最後部份我們藉由近場光學顯微術來分析聚焦高斯光束的輪廓並得到在繞涉極限之下的 100 奈米解析度。

Exploring New Functionalities of Scanning Optical Microscopy

Student：Yuen-Han Wang Advisors：Professor Jung Y. Huang

Department of Photonics and Institute of Electro-optical Engineering,
National Chiao Tung University

Abstract

This thesis presents the analysis of the modulation dynamics of surface stabilized ferroelectric liquid crystal (SSFLC) cells with a photon counting lock-in detection technology in the first section. This technique not only can effectively suppress the dc background of Raman spectrum, but also yields useful information about the modulation amplitudes and phases of specific Raman peaks. The SSFLC doped with ZnO nanocrystals was found to be switched with an electric modulation field in a more organized way than the undoped SSFLC and therefore has better resistance to the disordering effect caused by high frequency switching. This method provides conventional Raman spectroscopy with a new functionality for probing the spatial distribution and modulation dynamics of electro-optic active species in a thin film.

In the second section, we investigate the azimuthal dependence of Raman scattering attributed to high aspect ratio of nanorods and the image of phase-sensitive Raman scattering for monolayer 8CB molecule adsorbed on Ag nanorods array substrate by using photon-counting lock-in detection. In last section, we analyze the beam profile of a focused Gaussian beam and the resolution of spot size can be achieved to one hundred nanometers below the diffraction limit by using Scanning Near-field Optical Microscopy (SNOM) technology.

誌謝

在碩士研究過程中，首先非常感謝我的指導教授 黃中垚教授給予耐心與嚴謹的指導，雖然做此研究遇到些許問題而無法如期完成，但是在此段時間，也從教授的指導中學到更多解決問題的方法及研究的態度。

接著非常感謝我的家人，能夠讓我無後顧之憂的做研究，當我遇到困難時，給予我精神上的支持和自由而無所侷限，讓我有完成此研究之動力。

最後還要感謝實驗室的明彰學長、立志學長以及柳萱學姊的協助和指導，還有感謝秉寬、建輝、建佑的相處，讓我擁有這段多樣化且充滿回憶的日子。

CONTENTS

List of Table

LIST of FIGURES

Chapter 1

Introduction

Due to the minimum invasiveness to sample and the most intuitive image to our brain, optical microscopy (OM) had been developed into a convenient and useful tool for biology, chemistry and material science. Several optical processes had been used to form the optical image and reveal a variety of material properties. That enriches OM with many useful flavors, such as fluorescence microscopy, second-harmonic generation microscopy, third-harmonic generation microscopy and stimulated Raman Scattering microscopy. Although highly successful developments are abundant in OM, serious limitations on optical microscopy remain to be conquered. Abbe-Rayleigh criterion is one such limitation, which prevents two point sources with a lateral separation smaller than $\lambda/2$ from being resolved by any OM due to the intrinsic wavy nature of optical field. Unfortunately, a typical biomolecule has a dimension about 2 nm, which is two orders of magnitude below the Abbe-Rayleigh criterion on OM at visible light spectrum. There is high demand for OM with resolution surpassing the Abbe-Rayleigh criterion. Researchers around the world are making effort to achieve this goal by developing a variety of novel concepts.

In accompany with the development of super-resolution OM, developing new functionality for OM with an extremely weak signal has attracted significant research interest since its potential application in single molecular detection. In this thesis, we explore the possibility to enhance the functionality of OM.

In chapter 2, photon counting lock-in detected Raman imaging technique was employed to effectively suppress the nonresonant background of Raman spectrum and

information about the modulation amplitude and phase of specific Raman peak was yielded. The phase-sensitive detection of Raman signal reveals that the field-induced reorientation of nc-ZnO doped ferroelectric liquid crystal (FLC) film is more organized and therefore less sensitive to a high-frequency driving field.

In chapter 3, the photon-counting lock-in detection scheme was used to measure surface-enhanced Raman scattering (SERS) intensity of adsorbed molecules. The technique provides unique capability to deduce the orientation of tilted Ag nanorods, which shows the azimuthal distribution of the major axis of Ag nanorod projected on the x-y plane. Theoretical model of surface-enhanced Raman scattering (SERS) from a monolayer of molecules adsorbed on tilted silver nanorods was developed. The model allows us to deduce the polarizability tensor of a silver nanorod.

The key to a successful development of functional photonic devices lies in the fabrication and characterization. Valuable diagnostic tools not only improve our knowledge of photonic devices but also help to establish the design rules. Therefore, in this thesis study, we also developed a heterodyne interferometric scanning near field optical microscopy to reveal the full-field characteristics of photonic devices at the sub-wavelength region. In chapter 4, we described the preliminary results along this target.

In the rest part of this chapter, we review some technical background of the techniques to facilitate the description of this thesis.

a) Lock-in Detection

Lock-in detection is useful for the recovery of a weak signal embedded in a strong background. By using the lock-in detection scheme, we can obtain relationship between an excitation optical field and the emitted optical signal to characterize various molecules or materials. It yields important frequency-domain information about the response of the molecule perturbed by an external force.

Lock-in detection is a phase-sensitive detection (PSD) and can extract signal characteristics relative to a reference. Assuming the reference signal S_{ref} is a sinusoidal waveform with frequency ω_{ref} and phase ϕ_{ref} and the signal S_{ref} with frequency ω_{sig} and phase ϕ_{sig}

$$S_{ref} = A_{ref}\cos(\omega_{ref}t + \varphi_{ref}) \tag{1.1}$$

$$S_{sig} = A_{sig}\cos(\omega_{sig}t + \varphi_{sig}). \tag{1.2}$$

By multiplying Eq.(1.2) with Eq.(1.1), we obtain

$$\begin{aligned} X &= A_{ref}A_{sig}\cos(\omega_{ref}t + \varphi_{ref})\cos(\omega_{sig} + \varphi_{sig}) \\ &= \frac{1}{2}A_{ref}A_{sig}\cos[(\omega_{ref} + \omega_{sig})t + (\varphi_{ref} + \varphi_{sig})] \\ &+ \frac{1}{2}A_{ref}A_{sig}\cos[(\omega_{ref} - \omega_{sig})t + (\varphi_{ref} - \varphi_{sig})] \end{aligned} . \tag{1.3}$$

The signal detected with PSD is the two AC components, one at the difference frequency (ω_{ref}-ω_{sig}) and the other at the sum frequency (ω_{ref}+ω_{sig}). If ω_{ref}=ω_{sig} and reject the high frequency component with a suited band-pass filter, the output signal with difference frequency left

$$X = \frac{1}{2}A_{ref}A_{sig}\cos(\varphi_{ref} - \varphi_{sig}) \sim A_s\cos\theta. \tag{1.4}$$

If the reference signal is shifted by 90°, *i.e.* $A_{ref}\cos[(\omega_{ref}t + \phi_{ref} + 90^\circ)]$, the output will become

$$Y = \frac{1}{2}A_{ref}A_{sig}\sin(\varphi_{ref} - \varphi_{sig}) \sim A_s\sin\theta \quad . \tag{1.5}$$

The above signal processing algorithm can be implemented schematically in Fig. 1.1. By computing the magnitude of the signal vector, the phase dependency is removed. And the amplitude of the signal and the phase difference between reference and interesting signal can be obtained

$$R = \sqrt{(X^2 + Y^2)} = A_s$$

$$\theta = \tan^{-1}(Y / X)$$

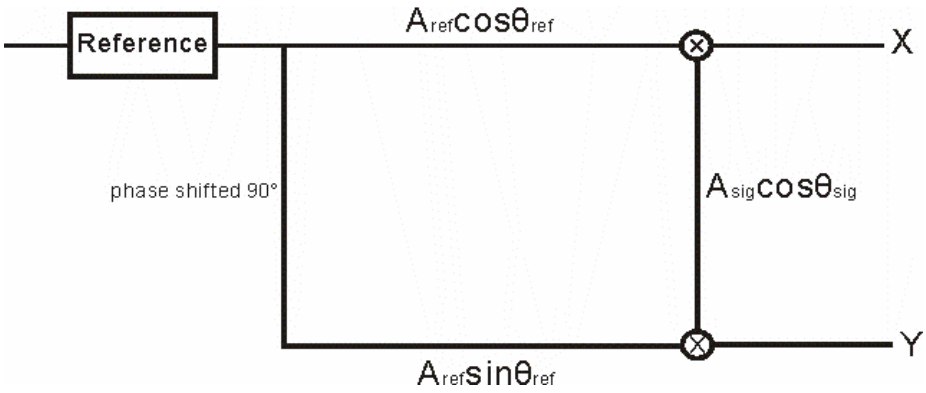

Fig. 1.1: Schematic of lock-in detection algorithm. By combining the output X and Y, we can extract the magnitude and the phase of interesting signal relative to that of the reference signal used.

b) Polarizable Nano Objects and Their Effects on Raman Scattering Process

Surface-enhanced Raman spectroscopy is a useful analytical tool for the detection of trace amount of molecules with capabilities of real-time monitoring and molecular specificity [1, 2]. The technique requires minimal sample preparation and is not destructive to sample. The enhancement effect of SERS arises from a substrate with rough metallic structure, such as nanoparticles, nanorods, nanoprisms, core-shell nano-structures, metallic nanohole or particle arrays [3, 4]. The morphology of the metallic structure plays an important role in determining the magnitude of signal enhancement.

Noble metallic nanoparticles, such as gold and silver, exhibit fairly strong surface plasmon resonance in the visible light range. The wavelength at which the surface plasmon resonance occurs is approximately constant for single isolated nanoparticle with size in the low nanometer range [5]. The interaction among nanoparticle arrays can be tunable [6, 7]. Adjusting the geometry or size of

nanoparticle enables tenability of the wavelength of optical resonance from visible to the near-infrared, which is presented in Fig. 1.2 and Fig. 1.3 [8].

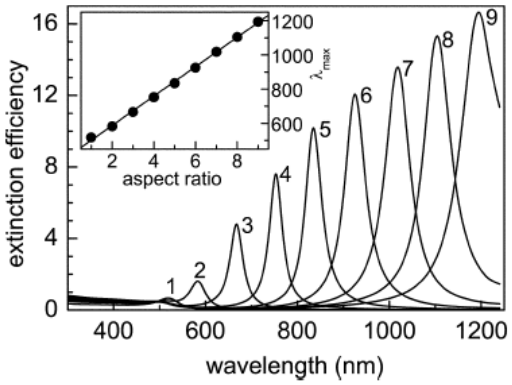

Fig. 1.2: The optical extinction of ellipsoidal gold nanoparticles, calculated by using the quasi-static approximation, with short radius β=5 nm and long radius α varying from 5 nm to 45 nm, corresponding to aspect ratios η=1-9 as indicated, is presented. The inset shows the wavelength of the longitudinal plasmon resonance peak as a function of aspect ratio. [**Ref. [8]**：E. Stefan Kooij and Bene Poelsema, *Phys. Chem. Chem. Phys.*, 8, 3349 (2006)]

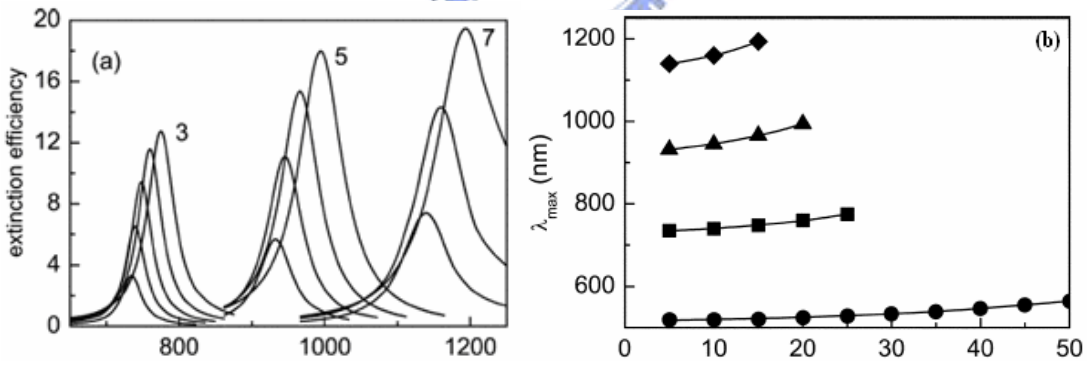

Fig. 1.3: (a) The optical extinction of ellipsoidal gold nanoparticle due to longitudinal plasmon resonance is calculated by using discrete dipole approximation and showed. For all aspect ratios, the smallest cylinders have a short diameter 2β= 5nm and long diameter 2α=15, 25, and 35 nm, corresponding to aspect ratio η=3, 5, and 7 as indicated, while the width is increased in steps of 5 nm. (b) The longitudinal peak as a function of cylinder width are showed for aspect ratios η=3 (square), 5 (triangles), and 7 (diamonds). And the size-dependence of surface plasmon resonance of spherical particles is also showed (circles) as a function of diameter, calculated by using Mie theory. [**Ref. [8]**：E. Stefan Kooij and Bene Poelsema, *Phys. Chem. Chem. Phys.*, 8, 3349 (2006)]

We can find that the wavelength of longitudinal plasmon resonant peak moves to long wavelength, *i.e.*, red-shift, when either the aspect ratio or size of ellipsoidal nanoparticle with low nanometers is increased. Besides, the extinction efficiency broadens with increasing ratio or size of ellipsoidal nanoparticle.

Early surface enhanced Raman scattering substrate included a random distribution of roughness produced by oxidation-reduction process on an evaporated thin metal film on a flat substrate [9]. The enhancement contributed from rough metallic structure is weak due to random distribution of roughness. Thus, many researches reported fabricating various nanostructures, such as rough metallic surface by chemical etching [10], silver nanoparticle array fabricated by lithography [11], and electro-deposition of silver on silver films at high potential [12], to improve SERS effect. However, those methods are either expensive, time consuming or irreproducible in preparing the desired surface morphology.

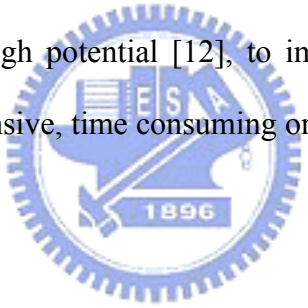

c). Oblique-Angle Deposition Technique

Oblique angle deposition (OAD) was proposed to fabricate metallic nanorods with the advantages of cheapness and time saving.

The oblique incidence of vapor atoms during evaporation can greatly alter the film properties was discovered simultaneously by Knorr, Hoffmann and Smith. The orientation and magnitude of the anisotropy in the resulting morphology of thin film depend on the deposition geometry used. When the angle between the incident direction of vapor atoms and the substrate normal is 45°, a shadowing effect becomes very effective to produce the anisotropy. In addition to the shadowing effect, surface diffusion was also found to be non-negligible [14].

Several models of oblique evaporation had been proposed in the literature to

model the morphology of columnar inclination, bundling and cross-sectional shape. For the inclination of columns, four mechanisms had been proposed to interpret the formation of tilted column from the oblique vapor incidence: (1) adaptation of the continuum model for finite atomic size, (2) shadowing, (3) conservation of parallel momentum, and (4) angle-dependent growth. Self-shadowing by surface rough or dust particle was found to play an important role for the effect of bundling. Behind nuclei or dust particle, there is empty area which can not be filled by incident vapor atoms. For cross-sectional shape, the conservation of parallel momentum is important in determining the shape of nuclei. Furthermore, by combining the conservation of momentum and relative oxygen concentration, the ratio between the number of oxygen and vapor atoms can vary along the nucleus contour, causes elongation of nuclei. To model the film texture, the main axes of crystal can change its direction by varying the incident angle of vapor atoms or other deposition parameters. At normal vapor incidence, there is only one planar reference, which is the plane of substrate. But at oblique incidence, the incident plane provides additional reference plane. As a result, textures with three degrees of freedom can be formed in oblique evaporation. Surface diffusion can play an important role in forming the texture. If surface diffusion is decreased significantly, the growth of crystal planes becomes highly dependent on the local incident angle of vapor atoms. There are several advantages for fabricating a layer of nanorods with oblique angle deposition: the controllable column angle, separation between bundling, size and shape of column and characteristic texture, *etc*. As a result, more and more researchers choose OAD to fabricate metallic nanostructured substrate.

Fig. 1.4 shows the top view and cross-sectional SEM image of a layer of silver nanorods [13]. We can see from the SEM images that the nanorods are not perfectly cylindrical with a variety of irregular shapes of corrugations, needles, and forks of

nanorods.

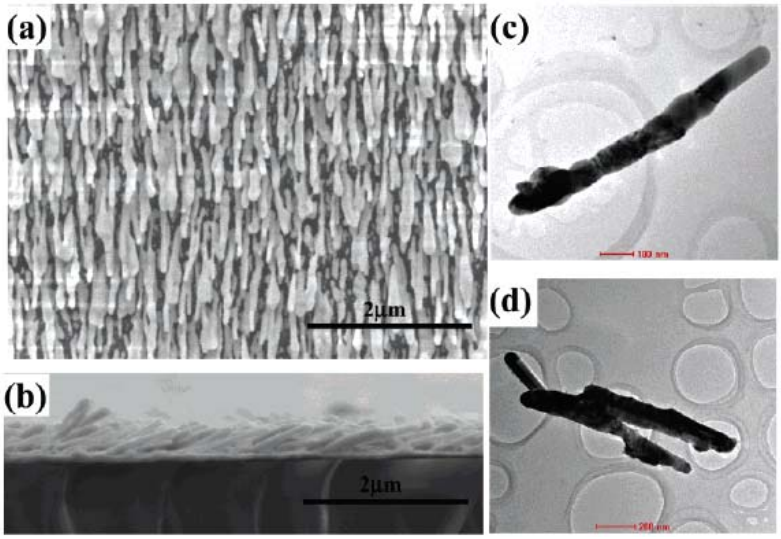

Fig. 1.4: (a) Top view and (b) the cross-sectional view SEM images of the sliver nanorods array on a glass slide. The scale bars represent 2 μm. the top view SEM was measured without additional metallic coating. (c) and (d) represent TEM image of individual silver nanorods. Scale bar is (c) 100 nm and (d) 200 nm. [**Ref. [13]**：Y.-P. Zhao, Stephen B. Chaney, Saratchandra Shanmukh, and Richard A. Dluhy**,** *J. Phys. Chem. B*, 110, 3153 (2006)]

Chapter 2

Raman Imaging of Surface-Stabilized Ferroelectric Liquid Crystal Film with Photon Counting Lock-in Detection

2.1 Introduction

Raman scattering is an inelastic scattering of a photon which creates (or annihilates) an optical phonon. When a photon bounces off a molecule, the inelastic scattered photon is less energetic and the associated light exhibits a frequency shift. The various frequency shifts associated with different molecular vibrations give rise to a spectrum, which is characteristic of a specific compound. Therefore, Raman spectroscopy has been widely used as a molecular fingerprinting probe to identify molecular species and structures of a complex material. Unfortunately, normal Raman signal not only is extremely weak with a signal at the single-photon counting level, but also is often overwhelmed with elastic scattered photons or fluorescent photons. Although lock-in detection is highly successful in recovering a weak electrical ac signal from large noise background, this phase-sensitive detection (PSD) scheme can not be directly applied to the detection of optical signal at photon counting level. Recently, a computer-based scheme had been developed to yield lock-in detection functionality with a conventional photon counting hardware for the detection of an extremely weak optical signal [15]. In this study, we combine the photon counting lock-in technique with Raman microscopy to probe the field-induced reorientation of an electro-optical switching surface stabilized ferroelectric liquid crystal (SSFLC) cell.

The ferroelectric liquid crystals FLCs have significant advantages for display applications compared to the widely used nematic liquid crystals such as the fast response time, wide viewing angle, and bistability of the two stable molecular orientations in the SSFLC molecular structures. [16, 17] We show that this Raman imaging scheme can successfully yield interesting information about the electro-optic active species that are closely related to the applications of SSFLC. Theoretical model of the phase-resolved Raman signal from a molecular normal mode was also formulated to illustrate the underlying principle.

2.2 Theoretical Background

The schematic of a SSFLC cell in a Raman scattering setup is depicted in Figure 2.1. Here Z denotes the rubbing direction, which is also the layer normal of the smectic layers of SSFLC. E is the applied electric field. The polarization angle of the polarized incident light E_L is taken as zero when its polarization direction coincides with the rubbing direction. M on the right diagram, which tilts from the molecular long axis ξ with an angle of β and rotates about the ξ-axis by γ, denotes the molecular normal mode responsible for the Raman scattering.

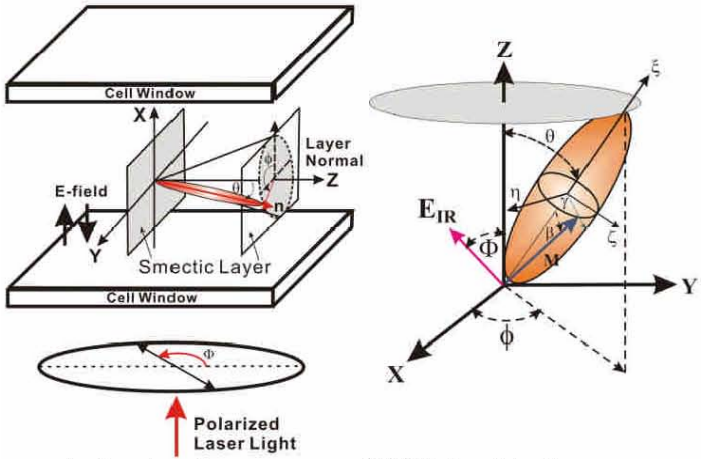

Fig. 2.1: Schematic of SSFLC cell: Z denotes the rubbing direction, which also the

layer normal of the smectic layers of SSFLC. E is the direction of the applied electric field. The polarization angle of the incident polarized light E_L is taken as zero when its polarization direction coincides with the rubbing direction. M on the right diagram denotes the IR dipole, which tilts from the molecular long axis ξ with an angle of β and rotates about the ξ-axis by γ.

The number of Raman scattered photons from FLC molecules is proportional to the square of projected Raman polarizability α_{ij}. Assuming α_{ij} for a normal mode with β=0 to be a tensor with single dominating component α_{MM}, the Y-polarized Raman signal (Φ=90°) excited by Y-polarized light is proportional to

$$R_{Y\to Y} = R_0 \sin^4\theta(3\sin\phi(t) + \sin[3\phi(t)])^4 \quad (2.1)$$

Similarly, the Z-polarized Raman signal (Φ=0°) is proportional to

$$R_{Y\to Z} = R_0 \sin^2(2\theta)\sin^2\phi(t)(2+\cos^2[2\phi(t)])^2 \quad (2.2)$$

By driving the SSFLC cell with a sinusoidal electric waveform of frequency Ω, the azimuthal angle φ(*t*) of FLC molecules on the SmC* cone can be modulated with an applied electric field *E*(Ω), which results in a modulated Raman signal from the electro-optical switching SSFLC cell.

For a theory of phase-sensitive detection (PSD), the analytical procedure of PSD at a given wavenumber ν typically involves a multiplication of the time-resolved Raman spectrum *R*(ν, t) with cos[Ωt + Ψ_{PSD}] followed by normalized integration over a period of T:

$$\overline{R}_{\phi_{PSD}}(\nu,\Omega) = \frac{2}{T}\int_0^T R(\nu,t)\cos(\Omega t + \Psi_{PSD})dt \quad (2.3)$$

Applying Eq. (2.3) to all wavenumber ν of the spectrum leads to a data vector where the time-resolved Raman spectra *R*(ν, t) and $\overline{R}_{\Psi_{PSD}}(\nu,\Omega)$ of Eq. (2.3) are treated like vector. Here $\overline{R}_{\Psi_{PSD}}(\nu,\Omega)$ is referred to as phase-resolved spectrum associated with

modulation frequency Ω and phase setting Ψ_{PSD}. For the special cases with Ψ_{PSD} =0° and Ψ_{PSD} =90°, $\overline{R}_{\Psi_{PSD}}(\nu,\Omega)$ is equivalent to the in-phase and out-of-phase components:

$$\overline{R}(\nu,\Omega)\cos[\Delta(\nu,\Omega)] = \overline{R}_{\Psi_{PSD}=0^\circ}(\nu,\Omega) = \frac{2}{T}\int_0^T R(\nu,t)\cos(\Omega t)dt$$
$$\overline{R}(\nu,\Omega)\sin[\Delta(\nu,\Omega)] = \overline{R}_{\Psi_{PSD}=90^\circ}(\nu,\Omega) = \frac{2}{T}\int_0^T R(\nu,t)\sin(\Omega t)dt \quad (2.4)$$

Here $\overline{R}(\nu,\Omega)$ and Δ(ν ,Ω) are the absolute modulation amplitude of the Raman signal and the corresponding phase shift. These are the main parameters important for the interpretation of a modulation experiment and can be determined from the measured phase-resolved spectra $\overline{R}_{\Psi_{PSD}=0^\circ}(\nu,\Omega)$ and $\overline{R}_{\Psi_{PSD}=90^\circ}(\nu,\Omega)$ by using

$$\overline{R}(\nu,\Omega) = \sqrt{\overline{R}_{\Psi_{PSD}=0^\circ}(\nu,\Omega)^2 + \overline{R}_{\Psi_{PSD}=90^\circ}(\nu,\Omega)^2}, \textit{with}$$
$$\sin[\Delta(\nu,\Omega)] = \overline{R}_{\Psi_{PSD}=90^\circ}(\nu,\Omega)/\overline{R}(\nu,\Omega) \quad (2.5)$$
$$\cos[\Delta(\nu,\Omega)] = \overline{R}_{\Psi_{PSD}=0^\circ}(\nu,\Omega)/\overline{R}(\nu,\Omega)$$

Thus, the purpose of the PSD in modulation spectroscopy is the evaluation of phase-resolved spectra $\overline{R}_{\Psi_{PSD}}(\nu,\Omega)$.

2.3 Experiment

The laser used in our Raman imaging apparatus with photon-counting lock-in detection is a 60 mW CW diode-pumped solid state laser operating at 532 nm. The laser was weakly focused with a lens of 20-cm focal length to yield an elliptical spot 90μm×60μm on the sample at an incident angle of 45°. The SSFLC cell was driven with a sinusoidal electric waveform of frequency Ω. The Raman scattered photons were collected with a lens, and filtered by using a Raman notch filter and a spectrograph. The photons were detected with a cooled photomultiplier tube and processed by a single-photon counting module. The lock-in amplitude and phase were

retrieved from the photon-counting pulses with the lock-in photon counting software developed by Dieter Braun [15].

The surface-stabilized ferroelectric liquid crystal (SSFLC) cells consist of two ITO-glass plates coated with polyimide alignment layers (RN1182 from Nissan Chemical), which had been rubbed undirectionally along the Z-axis as shown in Figure 1. The substrates were separated by 1.5μm-thick spacers to maintain a cell gap closing to the half-wave thickness $d_{\lambda/2} = \lambda / 2\Delta n \simeq 1.9\mu m$ estimated with $\Delta n \simeq 0.17$ and λ=0.633 μm. Felix 017/100, a FLC mixture from Clariant inc. (Germany), was used in view of its potential device applications [18].

The ZnO nanoparticles used had been caped with 3-(**t**rimethoxysilyl) propyl methacrylate (TPM) during the synthesis process of nc-ZnO. The bandgap and the photoluminescence peak of the TPM-caped ZnO nanocrystals were found to be 3.54 eV and 518 nm, indicating the averaged diameter of the nanoparticles to be about 3.2 nm [19]. An appropriate amount of *nc*-ZnO powder was added into the pure Felix 017/100 to 1.0% by weight. The mixture was homogenized with ultrasonic at 85℃ for 40 min and then cooled down to room temperature in vacuum. The desired FLC material in the isotropic phase was filled into the test cells and then the test cells were cooled slowly to 35℃ to yield a stable SmC* phase.

2.4 Results and Discussion

2.4.1. SSFLC Cell with Pure Felix 017/100

A SSFLC cell with pure Felix 017/100 was investigated first with Raman spectroscopy without applying an electric modulation field. The cell was excited with a Y-polarized 532-nm laser beam. The resulting dc Raman spectrum exhibiting clearly five major Raman peaks is presented in Fig. 2.2 (a). We can attribute these

peaks at 1610 cm^{-1}, 1505 cm^{-1}, and 1326 cm^{-1} to the C=C stretching modes of benzene ring, the 1446 cm^{-1} peak to the C=C stretch of pyrimidine ring, and the 1118 cm^{-1} to the C-O-C motion [20].

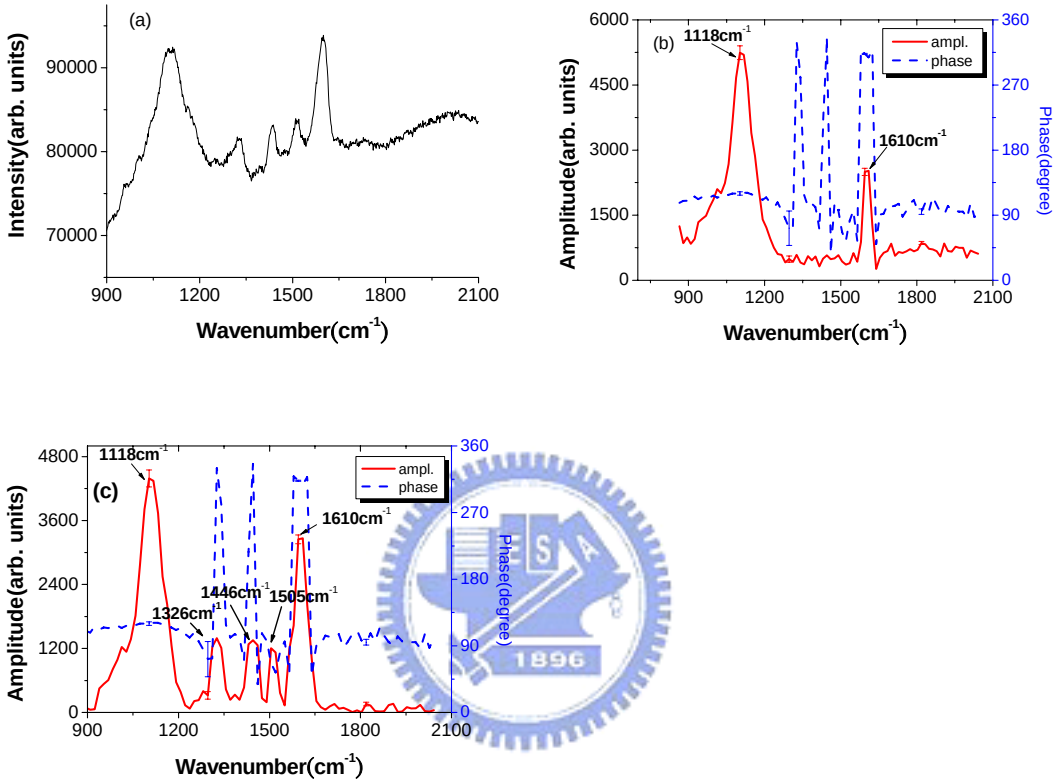

Fig. 2.2: (a) DC unmodulated Raman spectrum of a pure SSFLC cell excited at 532 nm. (b) The amplitude (solid curve) and phase (dashed line) profiles of a lock-in detected Raman spectrum $\overline{R}_{\Psi_{PSD}}(\nu,\Omega)$ with a modulation frequency Ω=250 Hz measured at the position p_1. (c) The corresponding lock-in detected amplitude (solid curve) after removing the nonresoant background.

When a photon-counting lock-in detection scheme is employed, the amplitude and phase of the Raman scattered light from the SSFLC cell driven by an electric field with a sinusoidal waveform of frequency Ω=250 Hz are presented in Fig. 2.2 (b). The nonresonant background clearly observable in Fig. 2.2 (a) is suppressed effectively by the lock-in detection scheme. The residual nonresonant signal is most likely to originate from the light scattering from the field-induced refractive index variation.

The three Raman peaks at 1326 cm^{-1}, 1446 cm^{-1}, and 1505 cm^{-1} disappear owing to the comparable amplitudes 180° phase difference with that of the nonresoant background. The phase of the nonresonant signal, which can be determined from the measured values in the nonresonant region, was found to be about 90°. By using the phase angle, we can remove the residual nonresonant background from the spectrum shown in Fig. 2.2 (b). The resulting lock-in detected Raman amplitudes (solid curve) are presented in Fig. 2.2 (c). The 90° phase angle of the nonresonant signal also causes the measured phase of Raman peak to vary from Δ~320° at 1610 cm^{-1}, to 60° at 1505 cm^{-1}, 180° at both 1446 cm^{-1} and 1326 cm^{-1}, and Δ~120° at 1118 cm^{-1}, depending upon their corresponding peak heights.

An optical transmittance image of the Felix 017/100 SSFLC cell is shown in Fig. 2.3 (a).Two defects can be observed in the scanned area of 1500μm×1500μm. The corresponding 2D distributions of the amplitude and the phase of the modulated Raman peak at 1610 cm^{-1} with Ω=250Hz are presented in Fig. 2.3 (b) and 2.3 (c). Both the dc Raman peak (not shown) and the modulated Raman signal amplitude at 1610 cm^{-1} (Fig. 2.3 (b)) are very weak inside the defects, indicating the defects to be voids without FLC molecules. To further verify the functionality of the lock-in detected Raman imaging technique, two sites (labeled by p1 and p2 in Figs. 2.3 (b) and 2.3 (c)) were chosen for further examination. Here the site 1 was chosen to reflect the general characteristics of the SSFLC cell and the site 2, which exhibits an enhanced electro-optic modulation response, was selected to reveal the influences on FLC from the rim of a void defect.

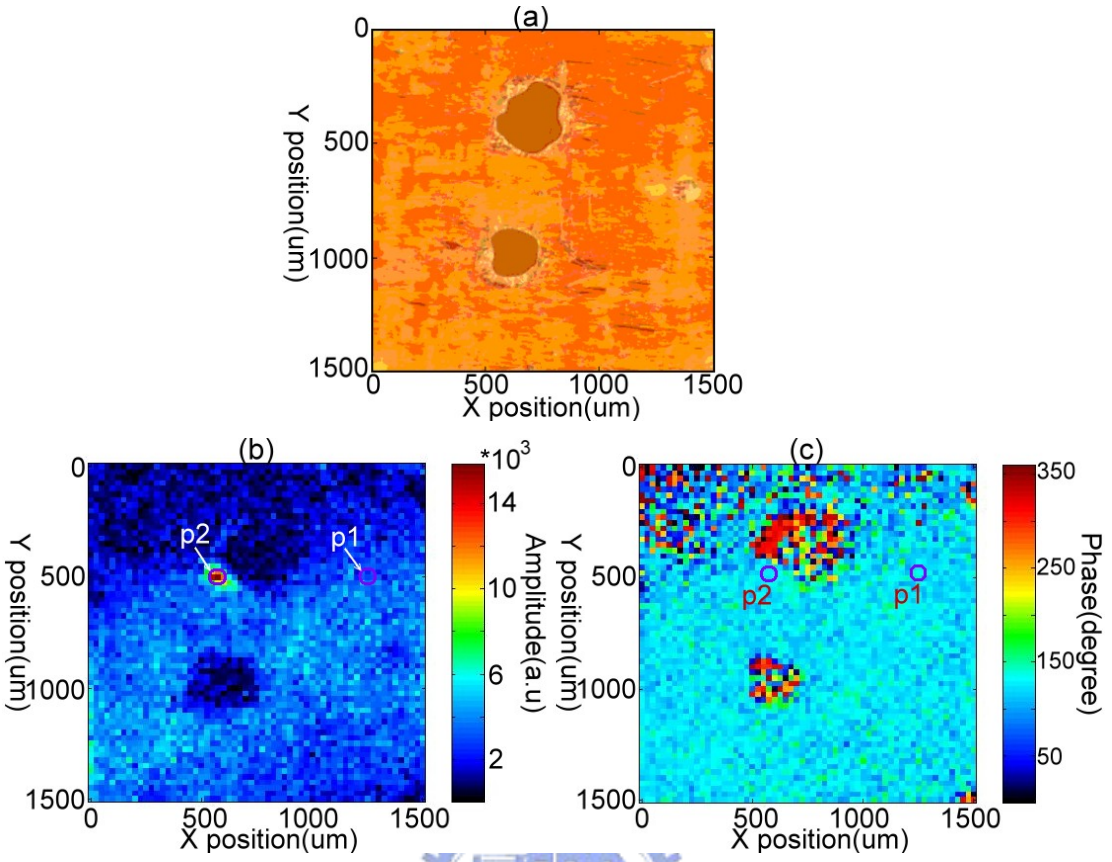

Fig. 2.3: (a) The optical transmittance image of a Felix 017/100 SSFLC cell, and the 2D distributions of (b) the amplitude, and (c) the phase of the lock-in detected Raman peak at 1609 cm^{-1} with a modulating frequency Ω=250Hz. Here p1 is the position of measured position 1 and p2 is the position of measured position 2.

In the frequency-domain, an SSFLC cell driven by a sinusoidal electric waveform can yield a change of the Raman scattered light and a phase shift between the scattered light and the driving waveform. The relationship between the driving field and the modulated Raman response can be expressed in terms of a transfer function $H(\Omega)$

$$\left|\frac{\Delta\bar{R}_{\Psi_{PSD}}(\nu,\Omega)}{\bar{R}_0(\nu)}\right| = H(\Omega)\left|\frac{\Delta E(\Omega)}{E_0}\right| = \left[\frac{1}{1-L\Omega^2+i\Omega\tau}\right]\left|\frac{\Delta E(\Omega)}{E_0}\right| \qquad (2.6)$$

Here E_0 is an appropriate normalization parameter for the driving field and $\bar{R}_0(\nu)$ is the DC intensity of the Raman peak, $\Delta E(\Omega)$denotes the AC amplitude of the driving electric field and $\Delta\bar{R}_{\Psi_{PSD}}(\nu,\Omega)$ the amplitude of phase-resolved Raman peak.

The experimental results of the 1118 cm^{-1}-peak from the position 1 as a function of modulation frequency Ω are presented in Fig. 2.4 (a). The measured phases of the modulated Raman response are shown with open symbols and the measured magnitude shown with filled symbols. Since the transfer function of modulation phase can only be affected by the modulation dynamics, we therefore determine the phase relaxation time from the fit of the measured phase of the Raman response at 1118 cm^{-1} to Eq. (2.6). The fitting results in a relaxation time of 6.27×10^{-3} sec. Unlike to the phase relaxation process, the magnitude of the modulated Raman response can be affected by either the modulation dynamics of the FLC molecules or the FLC molecular alignment (see Eqs. (2.1-2.2)). Since the FLC molecules could be aligned to form a lower ordered structure with a high-frequency driving field, a modulus transfer function with shorter relaxation time (and therefore wider 3-dB bandwidth) than that revealed by the phase function shall be revealed. This is exactly what we had observed in Fig. 2.4 (a), where the modulus transfer function of the modulated Raman response can be fitted to a solid curve with $\tau=1.54\times10^{-3}$ sec, which is about 4 times shorter than that (dashed curve) with the phase relaxation time $\tau=6.27\times10^{-3}$ sec. The reduction factor from the phase relaxation time to the magnitude relaxation time becomes a useful parameter to reflect the disordering effect of the FLC alignment from the high-frequency driving condition.

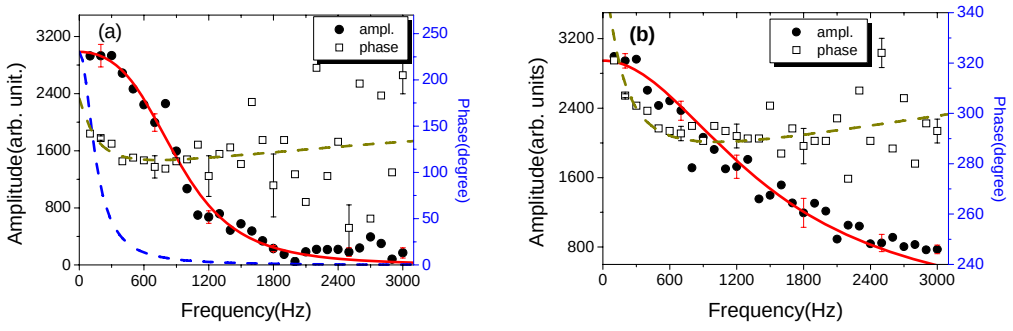

Fig. 2.4: The amplitude (filled circles) and phase (open squares) of a phase-resolved

Raman peak (a) at 1118 cm^{-1} and (b) at 1610 cm^{-1} at position 1 are presented as a function of modulated frequency Ω in a pure SSFLC cell and the solid curve is the fitting curve.

The experimental results of the 1610 cm^{-1}-peak from the position 1 as a function of Ω are presented in Fig. 2.4 (b). The relaxation time of the modulated Raman magnitude is deduced to be 6.7×10^{-4} sec, which is about 8.7 times shorter than the corresponding phase relaxation time 5.8×10^{-3} sec. A large reduction factor for the 1610 cm^{-1}-peak indicates that the disordering effect at high-frequency driving is more distinctive for the more rigid C=C stretching mode.

The modulus transfer function of the modulated Raman response at 1118 cm^{-1} at the position 2 yields a relaxation time of 6.05×10^{-3} sec, which is about 4.9 times shorter than the measured phase relaxation time 1.23×10^{-3} sec. The relaxation time for the 1610 cm^{-1}-peak from the position 2 decreases from 5.53×10^{-3} sec (phase) to 5.44×10^{-4} sec (amplitude), which is even larger (10.2) than that (8.7) from the position 1, revealing clearly the influence on FLC from the rim of a void defect.

2.4.2. Felix 017/100 SSFLC Cell Doped with nc-ZnO

We reported in our previous study that the electro-optical response of FLC can be improved by doping with zinc oxide nanocrystals [21]. This method opens up an effective nonsynthetic way to yield promising new FLC materials.

The optical transmittance image of a Felix 017/100 SSFLC doped with nc-ZnO cell is shown in Fig. 2.5 (a). The 2D distributions of the amplitude and the phase of the lock-in detected Raman signal at 1610 cm^{-1} with a modulated frequency 250 Hz are presented in Fig. 2.5 (b) and 2.5 (c). The optical image shown in Fig. 2.5 (a) indicates the lower right portion of the scanned area to be different from the rest part. Fig. 2.5 (b) reveals that FLC in this region produces weaker modulated Raman peak, indicating that the FLC is disordered to result in weaker electro-optical response. Two

sites labeled with p1 and p2 were chosen for further examination. Position 1 represents a location with general characteristics and position 2 was selected to reveal the structure with enhanced electro-optical response.

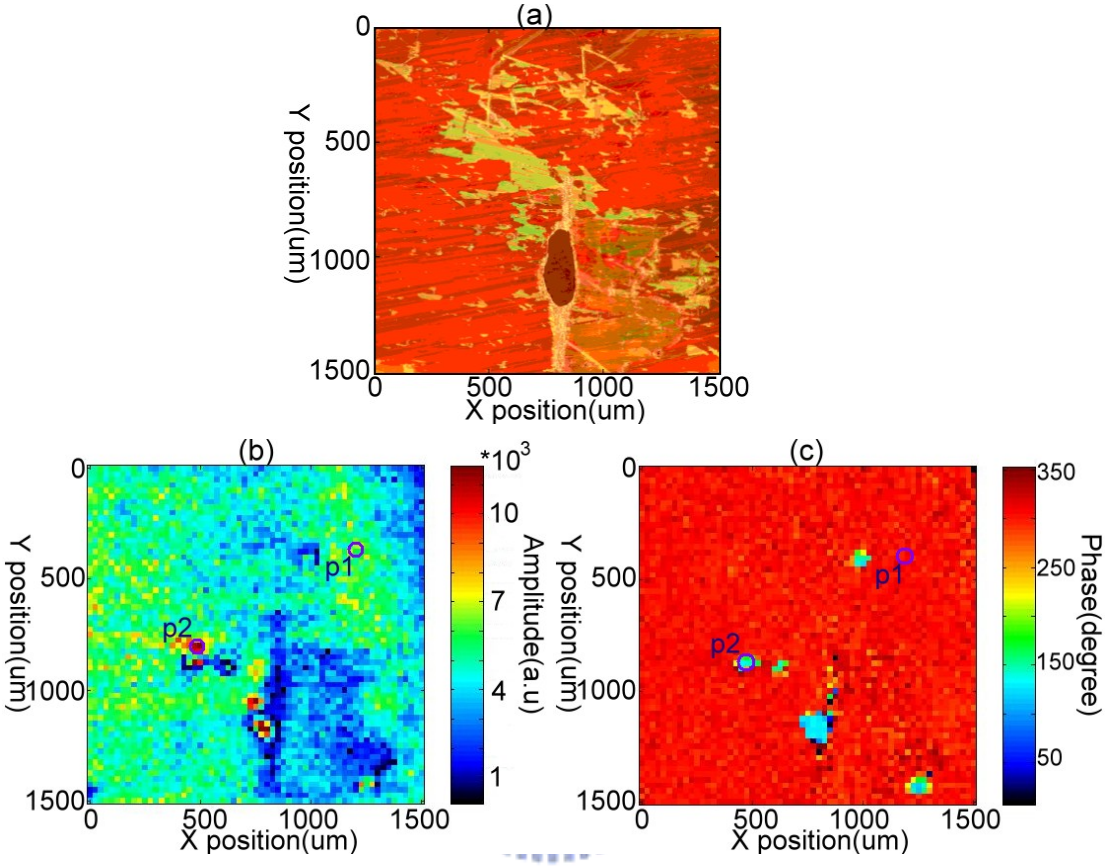

Fig. 2.5: (a) The optical image of scanned region is taken on a Felix 017/100 SSFLC cell doped with nc-ZnO by using optical microscopy, and the 2D distributions of (b) the amplitude, and (c) the phase of the lock-in detected Raman peak at 1609 cm^{-1} with a modulated frequency Ω=250Hz. Here p1 is the position of measured position 1 and p2 is the position of measured position 2.

The dc Raman spectrum of the nc-ZnO doped SSFLC cell excited with a Y-polarized laser beam at 532 nm is presented in Fig. 2.6 (a). The Raman spectrum is very similar to that shown in Fig. 2.2(a), except that the 1118 cm^{-1} peak from the C-O-C motion is weaker while the C=O group at 1763 cm^{-1}, which contributes to the nonvanishing spontaneous polarization of this FLC material in SmC*, is more distinctive. When the photon counting lock-in detection is employed, the amplitude and phase of the lock-in detected Raman spectrum with a sinusoidal waveform of

Ω=250 Hz are presented Figs. 2.5 (b). The phase of the nonresonant signal was found to be about 330°. By using the phase angle, we can remove the nonresonant background from the spectrum shown in Fig. 2.5 (b). The resulting lock-in detected Raman amplitudes (solid curve) are presented in Fig. 2.5 (c). The modulated Raman signal exhibits a phase angle Δ~330° at 1610 cm^{-1} and Δ~140° at 1118 cm^{-1}, which are similar to that of Fig. 2.2 (b). However, the phase of the C=C stretching modes was found to be about 330°, which is in phase with the nonresonant signal. As pointed out previously, the nonresonant signal is most likely to originate from the light scattering from the field-induced refractive index variation. The zero phase difference between the modulated nonresonant signal and the C=C stretching peaks suggests that doping SSFLC with *nc*-ZnO appears to result in a more organized field-induced reorientation process.

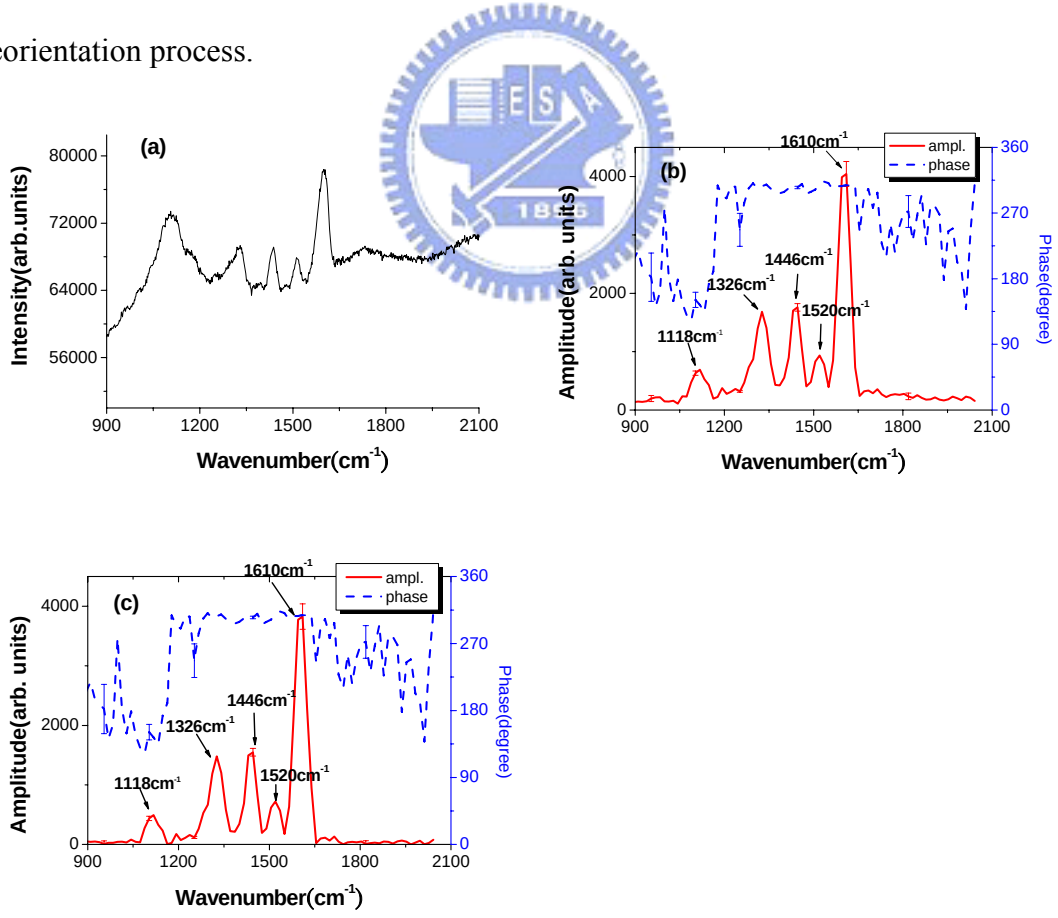

Fig. 2.6: (a) DC unmodulated Raman spectrum of a SSFLC cell doped with *nc*-ZnO excited at 532 nm. (b) The amplitude (solid curve) and phase (dashed line) profiles of

a lock-in detected Raman spectrum $\overline{R}_{\Psi_{PSD}}(\nu,\Omega)$ with a modulation frequency Ω=250 Hz measured at the position p_1. (c) The corresponding lock-in detected amplitude (solid curve) after removing the nonresoant background.

The measured transfer function of the Raman peak at 1610 cm^{-1} from the positions 1 and 2 are presented in Figs. 2.7 (a) and 2.7 (b). The solid curves are the fitting results to Eq. (2.6). The relaxation time deduced from the measured magnitude at 1610 cm^{-1} from the position 1 is 9.89×10^{-4} sec, which is about 5 times shorter than 4.98×10^{-3} sec of the phase relaxation time. At position 2 (Fig. 2.7 (b)) the amplitude relaxation time becomes 6.81×10^{-4} sec, which is about 3.5 times shorter than the corresponding phase relaxation time 2.36×10^{-3}. Since the reduction factor from the phase relaxation time to the amplitude relaxation time is useful to reflect the disordering effect in the FLC alignment originating from high-frequency switching. Our results indicate that the field-induced reorientation dynamics of the nc-ZnO doped SSFLC film at the position 2 is more organized and therefore less sensitive to the high-frequency driving induced disordering.

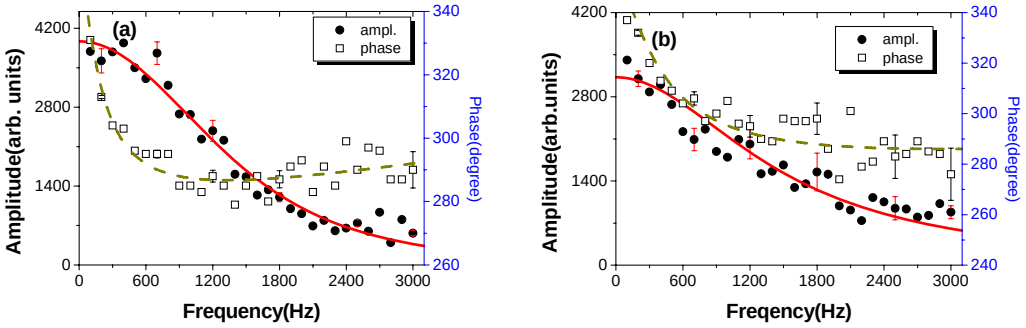

Fig. 2.7: The amplitude (triangle symbols) and phase (circular symbols) of a phase-resolved Raman peak at 1609 cm^{-1} (a) at position1 and (b) at position 2 are presented as a function of modulated frequency Ω in a SSFLC doped with nc-ZnO cell and the solid curve is the fitting curve.

2.4.3. CV Characteristics of Felix 017/100 SSFLC Cells

When an electric field is applied along the polarization axis of a SSFLC cell, the

orientation of the FLC molecules is changed. The FLC molecules can be aligned parallel or antiparallel to the positive field direction. The transition from the antiparallel state to the parallel state is accompanied with a change in the direction of polarization. This gives rise to a nonlinear contribution to the capacitance value of the ferroelectric. Hence the ferroelectric capacitance consists of linear as well as nonlinear parts [22]

$$C_{LC} = C_{lin} + (\frac{dp}{dV_{ext}})\frac{A}{d} \tag{2.7}$$

where C_{lin} denotes the linear capacitance, V_{ext} the applied voltage, A and d the area and the thickness of the capacitor, respectively. The nonlinear part of the FLC capacitance relating to the polarization reversal can be deduced by using the Preisach model, which assumes that the individual dipoles of the FLC film add up to yield the total polarization and each of them exhibits a rectangular hysteretic loop. The external applied field can interact with the dipoles and changes their directions.

Assuming the direction of the dipoles in thermal equilibrium to follow a Gaussian distribution, the total polarization P of the FLC film can then be expressed as [23]

$$P(V_{ext}) = FP\tanh[\delta(V_{ext} \simeq V_c^{\pm})] \tag{2.8}$$

Here the parameter F is used to depict the non-saturated behavior of the loop; δ is a constant with

$$\delta = \log(\frac{1+\mathrm{P_r}/P_s}{1-\mathrm{P_r}/P_s})/V_c \tag{2.9}$$

$\mathrm{P_s}$ denotes the saturated polarization (or the spontaneous polarization), and $V_c^{\pm}$ is the mean value of the individual coercive voltage. The (+) sign refers to an increase of V_{ext}, and the (-) sign indicates a decrease of V_{ext}. ($\mathrm{FP_s}$) carries the meaning of the proportion of the dipoles in the nonsaturated switching loop [24]. By combining Eq.

(2.7) with (2.8), the FLC capacitance with multiple dipolar species can be expressed as

$$C_{LC} = C_{lin} + \sum_i \frac{(FP_s)_i \delta_i}{\cosh^2(\delta_i (V_{ext} \simeq V_{Ci}^{\pm}))} \frac{A}{d} \tag{2.10}$$

Eq. (2.10) shows that the capacitance peak in the C-V curve shall coincide with the polarization reversal point with the peak height relating to the amount of switchable polarization [25].

Figure 2.8 (a) shows the measured data of the undoped SSFLC (open circles) and the *nc*-ZnO doped SSFLC (filled triangles) at an applied field frequency of 1 kHz. The corresponding fitting curves to Eq. (2.10) are presented with solid lines. As shown in the Fig. 2.8 (a), the undoped SSFLC cell needs three Preisach terms to yield a satisfactory fit, while for the doped SSFLC only one term is sufficient. This result suggests that ZnO nanocrystals effectively tie together the surrounding FLC dipolar species and simplify their field-induced switching behaviors. The sub molecular binding effect is possible in view that ZnO nano dots possess fairly large dipole moments and can interact the FLC molecules via dipolar interaction.

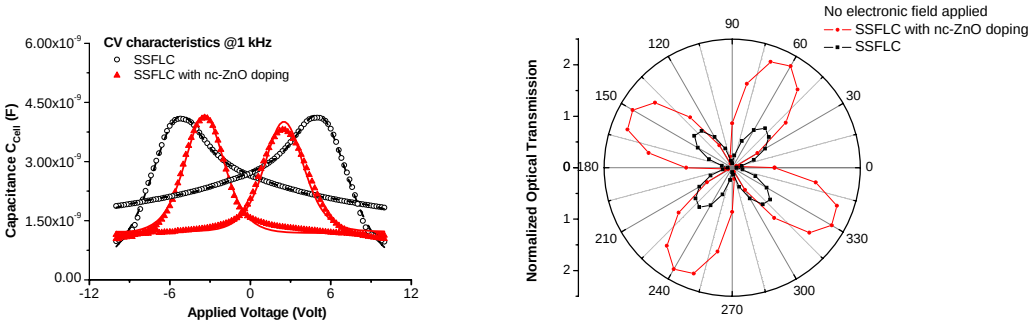

Fig. 2.8: (a) The experimental C-V curves (symbols) and their fitting results (solid lines) of the SSFLC cells without and with *nc*-ZnO doping at 1 kHz. (b) The normalized transient electro-optical azimuthal patterns of the pure SSFLC (open squares) and the SSFLC with nc-ZnO doping (filled circles) cells are presented without an electric field.

The patterns of normal optical transmittance through the undoped (open symbols) and the doped (filled symbols) SSFLC cells, which were positioned between a crossed polarizer-analyzers setup, are presented in Figure 2.8 (b). By rotating the SSFLC cells about the beam propagation direction, an azimuthal pattern with four-folded lopes was observed [26]. The dark state has a fairly small light leakage, indicating that both of the two SSFLC cells possess fairly high quality of molecular alignment. The bright state of the doped SSFLC cell yields 2.6 times larger optical transmittance than that of the undoped cell. The result supports the notion that the intermolecular binding effect via nc-ZnO doping produces a higher ordered alignment to result in an improved optical transmissive property.

2.5 Conclusion

In summary, we had applied photon counting lock-in detected Raman imaging technique to investigate the modulation dynamics of surface stabilized ferroelectric liquid crystal with or without doping of ZnO nanocrystals. The technique not only effectively suppresses the nonresonant background of Raman spectrum, but also yields the information about the modulation amplitude and phase of specific Raman peak. The reduction factor from the phase relaxation time to the amplitude relaxation time is useful to reflect the disordering effect of the FLC alignment from the high-frequency driving. The field-induced reorientation dynamics of the nc-ZnO doped SSFLC film is generally more organized and therefore less sensitive to the high frequency driving induced disordering. The result is also supported by the CV characterization. We propose the ZnO nano dots to act as an effective molecular binder by tieing together surrounding FLC dipolar species and yield a 2.5-time improvement in the optical transmittance of *nc*-ZnO-doped SSFLC. The method

reported here opens up an effective non-synthetic way to yield promising new FLC materials.

Chapter 3

Lock-In Detected Raman Microscopy of Liquid Crystal Molecules on Tilted Silver Nanorods

3.1 Introduction

The phenomenon of inelastic light scattering by molecular vibration was discovered by C. V. Raman in 1928. To observe this effect, an optical beam is used to illuminate a material and the scattered photons are detected with the help of a sensitive photon detector and a spectrograph. The scattered photons are frequency shifted from the incident excitation photons. The frequency-shifted optical signal consists of two components, the scattering process leading to red-shift frequency is called Stoke scattering and that with blue-shift frequency is called anti-Stoke scattering. The spontaneous Raman scattering is a rather weak process. The intensity of spontaneous Raman signal is orders of magnitude weaker than fluorescence. Surface enhanced Raman scattering (SERS) was discovered thirty years ago [27,28] with the capability to detect a monolayer of molecules adsorbed on roughened noble metal electrodes. Afterwards the technique was developed into a powerful and sensitive spectroscopic tool for chemical analysis. This technology usually utilizes rough metallic surfaces, such as nanoparticles, core-shell nanostruture and nanorods, to yield local field enhancement with plasmon resonance. Due to their extremely high aspect ratio, nanorods and nanowires were found to be effective in producing SERS [13, 29].

In this chapter, surface enhanced Raman scattering from a monolayer of cyano biphenyl (8CB) liquid crystal molecules adsorbed on a tilted silver nanorods coated substrate is studied theoretically and experimentally. The tilted Ag nanorods were

fabricated with oblique angle deposition (OAD) technique [30]. OAD belongs to a physical vapor deposition process in which the incident atoms are deposited on a substrate at a large incident angle with respect to the surface normal of the substrate. By using oblique angle deposition to fabricate tilted nanorods, the size and shape of nanorods can be controlled. The tilt angle of nanorods with respect to the surface normal and the texture in an oblique angle deposited film can be adjusted.

3.2 Theoretical Analysis of Surface Enhanced Raman Scattering From Adsorbed Molecules on a Layer of Ag Nanorods

3.2.1 Mie-Scattering

Light scattering occurs as long as there is fluctuation in the optical property of material. Considering that a dielectric particle with a polarizability of $\tilde{\alpha}(\omega)$ is exposed to a polarized optical field $\vec{E}_0$, the induced dipole $\vec{p}$ becomes

$$\vec{p}(\omega) = \tilde{\alpha}(\omega) \cdot \vec{E}_0 \qquad (3.1)$$

The polarizability depends on the shape and size of particle, the optical property of material and the optical frequency used. Due to the time-varying behavior of the incident optical field, the induced dipole moment oscillates and can radiate at the oscillating frequency.

For a silver rod with a length of ~2000 nm and diameter of ~100 nm, its polarizability can be expressed as [27]

$$\ddot{\alpha}_r = \begin{bmatrix} \alpha_{11} & \alpha_{21} & \alpha_{31} \\ \alpha_{21} & \alpha_{11} & \alpha_{31} \\ \alpha_{31} & \alpha_{31} & \alpha_{33} \end{bmatrix}. \tag{3.2}$$

In view of the geometrical symmetry and physical properties of the nanorod, there are only four independent components instead of nine in a general case. The schematic of Mie scattering from Ag nanorods is presented in Fig. 3.1.

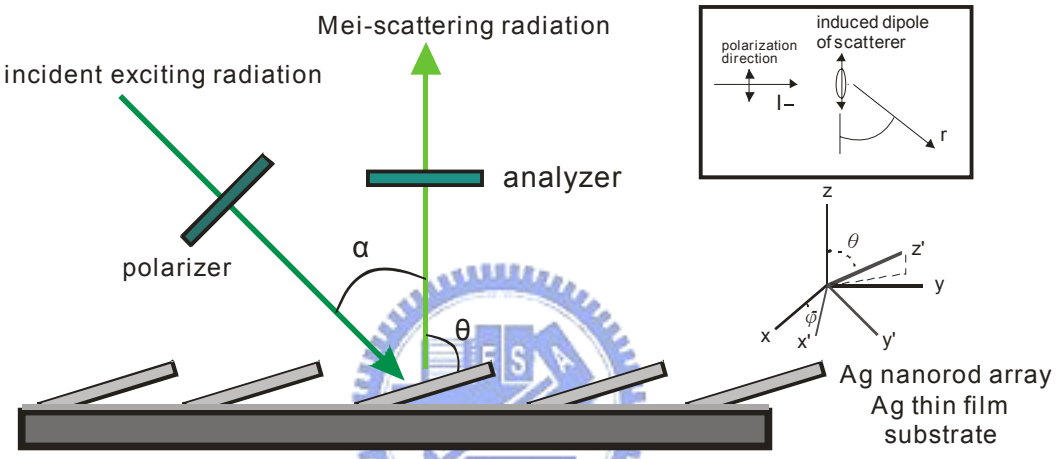

Fig. 3.1: Schematic of Mie scattering from a substrate coated with tilted Ag nanorods. An incident polarized optical beam excites the silver nanorods to produce induced dipoles and an optical analyzer located in front of detector is used to analyze the polarization of the scattering signal.

In Fig.3.1, we project the incident optical field in the laboratory coordinate system (x, y, z) onto the coordinate system (x', y', z') of Ag nanorod, where z'-axis is aligned to parallel to the long axis of the nanorod. The relationship between the laboratory coordinates system and the nanorod's coordinates system is described by the transformation $\ddot{T}$

$$\ddot{T} = \begin{bmatrix} 1 & 0 & 0 \\ 0 & \cos\theta & -\sin\theta \\ 0 & \sin\theta & \cos\theta \end{bmatrix} \begin{bmatrix} \cos\varphi & \sin\varphi & 0 \\ -\sin\varphi & \cos\varphi & 0 \\ 0 & 0 & 1 \end{bmatrix} = \begin{bmatrix} \cos\varphi & \sin\varphi & 0 \\ -\cos\theta\sin\varphi & \cos\theta\cos\varphi & -\sin\theta \\ -\sin\theta\sin\varphi & \sin\theta\cos\varphi & \cos\theta \end{bmatrix}, \tag{3.3}$$

where θ denotes the angle between the z- and z'-axis and ϕ is the angle between the x- and x'-axis. The incident optical field in the nanorod's coordinate system can then be found to be

$$\vec{E}_0' = \begin{bmatrix} E_{0x}' \\ E_{0y}' \\ E_{0z}' \end{bmatrix} = \vec{\vec{T}} \cdot \vec{E}_0 \quad , \tag{3.4}$$

The Mie scattering intensity by Ag nanorod can be written as

$$I_{sca} = \left| \hat{e}_s \cdot \vec{\vec{T}}^{-1} \cdot \vec{\vec{\alpha}}_r \cdot \vec{\vec{T}} \cdot \hat{e}_i \right|^2 , \tag{3.5}$$

where $\hat{e}_i$ and $\hat{e}_s$ are the unit vectors of the incident optical exciting field and the Mie scattering field in the laboratory coordinates system. In the simplest case, the polarizability of the silver nanorod can be a diagonal form when the induced dipoles can only be generated to along to the direction of optical field. However, an induced dipole perpendicular to the optical field may be produced by a more general optical driving pattern of valence electrons. In the case of our silver nanorod, the non diagonal terms of $\vec{\vec{\alpha}}_r(\omega)$ turn out to be non negligible.

3.2.2 Surface Enhanced Raman Scattering From Tilted Ag Nanorod

When the molecule of interest is located closed to a polarizable body, the effect of the electromagnetic interaction will occur. The effective electric field $\vec{E}$ experienced by the molecule is composed of the incident polarized radiation $\vec{E}_0$ and a dipole field from the nearby induced dipole. In Fig. 3.2, the schematic of surface enhanced Raman scattering is presented. In brief, two kinds of Raman scattering field are taken into account: one is the direct Raman scattering from the molecule of interest without nanorod and the other is an indirect Raman scattering from an

interaction between adsorbed molecule and nanorod [28].

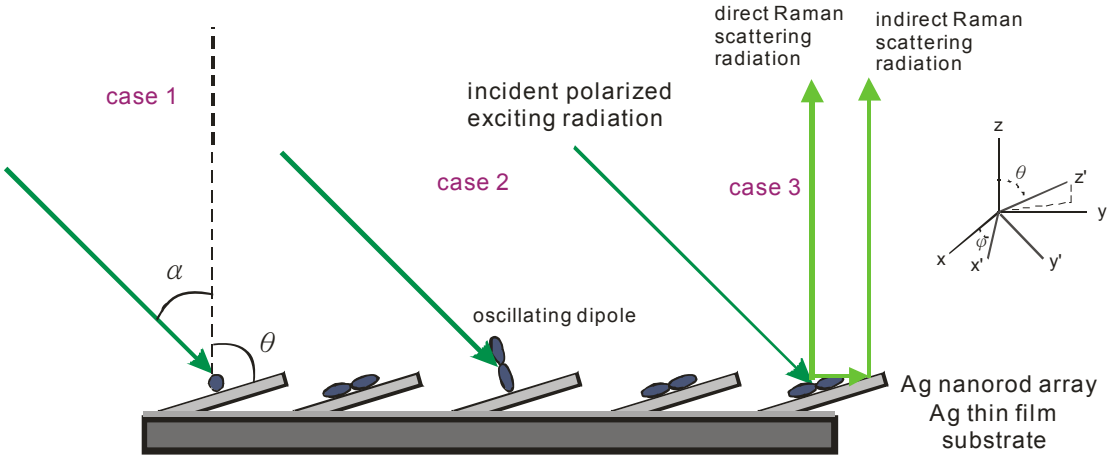

Fig.3.2: Schematic of surface enhanced Raman scattering from a substrate coated with tilted Ag nanorods.

We describe the molecular polarizability with $\ddot{\alpha}_m$ and the nearby polarizable body is a silver nanorod with polarizability $\ddot{\alpha}_r$. This leads to induced dipoles with the following expressions:

$$\begin{aligned}\vec{P}_m &= \ddot{\alpha}_m \cdot \vec{E} = \ddot{\alpha}_m \cdot (\vec{E}_0 + \ddot{M} \cdot \vec{P}_r) \\ \vec{P}_r &= \ddot{\alpha}_r \cdot \vec{E} = \ddot{\alpha}_r \cdot (\vec{E}_0 + \ddot{M} \cdot \vec{P}_m)\end{aligned}, \qquad (3.6)$$

where $\vec{P}_m$ and $\vec{P}_r$ are the induced electric dipole of the molecule and nanorod, respectively; $\ddot{M} = (3\hat{n}\hat{n} - \ddot{I})/d^3$ with $\vec{d}$ denoting the distance between the molecule and the center of mass of the nanorod; $\hat{n} = \vec{d}/d$; and $\ddot{I}$ a unit tensor. By expressing Eq. (3.6) in terms of the incident optical field $\vec{E}_0$, we obtain

$$\begin{aligned}\vec{P}_m &= \ddot{\alpha}_m^{eff} \cdot \vec{E}_0 = (\ddot{I} - \ddot{\alpha}_m \cdot \ddot{M} \cdot \ddot{\alpha}_r \cdot M)^{-1} \cdot \ddot{\alpha}_m \cdot [\ddot{I} + \ddot{M} \cdot \ddot{\alpha}_r] \cdot \vec{E}_0 \\ \vec{P}_r &= \ddot{\alpha}_r^{eff} \cdot \vec{E}_0 = (\ddot{I} - \ddot{\alpha}_r \cdot \ddot{M} \cdot \ddot{\alpha}_m \cdot \ddot{M})^{-1} \cdot \ddot{\alpha}_r \cdot [\ddot{I} + \ddot{M} \cdot \ddot{\alpha}_m] \cdot \vec{E}_0\end{aligned}. \qquad (3.7)$$

By choosing a large enough value of d to remove high-order terms, Eq. (3.7) is

reduced to

$$\vec{P}_m = \ddot{\alpha}_m^{eff} \cdot \vec{E}_0 = \ddot{\alpha}_m \cdot [\ddot{I} + \ddot{M} \cdot \ddot{\alpha}_r] \cdot \vec{E}_0$$
$$\vec{P}_r = \ddot{\alpha}_r^{eff} \cdot \vec{E}_0 = \ddot{\alpha}_r \cdot [\ddot{I} + \ddot{M} \cdot \ddot{\alpha}_m] \cdot \vec{E}_0 \quad . \tag{3.8}$$

Notice that the Raman polarizability α_m can be associated with normal mode coordinates, the total Raman polarizability becomes

$$\ddot{\alpha}_{Raman}^{tot} = \Delta Q \frac{\partial}{\partial Q}[\ddot{\alpha}_m^{eff} + \ddot{\alpha}_r^{eff}] = \Delta Q[\frac{\partial \ddot{\alpha}_m}{\partial Q} + \frac{\partial \ddot{\alpha}_m}{\partial Q} \cdot \ddot{M} \cdot \ddot{\alpha}_r + \ddot{\alpha}_r \cdot \ddot{M} \cdot \frac{\partial \ddot{\alpha}_m}{\partial Q}]. \tag{3.9}$$

The total Raman scattering intensity from the molecules adsorbed on Ag nanorods is given by

$$I \propto \left| \hat{e}_R \cdot \ddot{T}^{-1} \cdot \ddot{\alpha}_{RAM}^{tot} \cdot \ddot{T} \cdot \hat{e}_i \right|^2, \tag{3.10}$$

where $\hat{e}_i$ and $\hat{e}_R$ are the unit vectors of the incident exciting field and the Raman scattering field in the laboratory coordinates system.

There are three geometries for the molecules to lie on the silver nanorods: In the case 1, where the long axis of adsorbed molecule lies along to the x'-axis of the nanorod coordinates system, the probability for a molecule to take this adsorbed geometry is assumed to be $\rho_{x'}$. The resulting polarizability $\ddot{\alpha}_m$ becomes

$$\ddot{\alpha}_m = \begin{bmatrix} \alpha & 0 & 0 \\ 0 & 0 & 0 \\ 0 & 0 & 0 \end{bmatrix} . \tag{3.11}$$

Inserting Eq. (3.11) into Eq. (3.9) and Eq. (3.10), the Raman scattering intensity from the adsorbed molecule in this case is denoted by I_1. Similarly, for the case 2 where the long axis of adsorbed molecule lies along to the y'-axis of the nanorod coordinates system, the probability for a molecule to take this adsorbed geometry is $\rho_{y'}$. The Raman scattering intensity is denoted by I_2. And for the case 3 where the long axis of adsorbed molecule is along to the z'-axis of the nanorod coordinates system, the

probability for a molecule to take this adsorbed geometry is $\rho_{z'}$. The Raman scattering intensity is I_3. Thus, when we take into account the three cases, the total Raman scattering intensity I_{tot} shall be equal to

$$I_{tot} = \rho_{x'} I_1 + \rho_{y'} I_2 + \rho_{z'} I_3 \quad . \tag{3.12}$$

3.3 Experimental Apparatus of Surface Enhanced Raman Spectroscopy

The nanorods coated substrate is prepared with oblique-angle vapor deposition (OAD) method as detailed by Dr. Zhao, *et al*. [31]. It was made with 20-nm Ti, 500-nm Ag film and a layer of 2000-nm long silver nanorods. We deposited a drop of 30 μM 8CB/Isopropyl Alcohol (IPA) solution on the Ag nanorods-coated substrate, a monolayer of 8CB molecule will be formed. The apparatus used for acquiring polarization-modulating Raman spectrum of 8CB monolayer is depicted in Fig. 3.3.

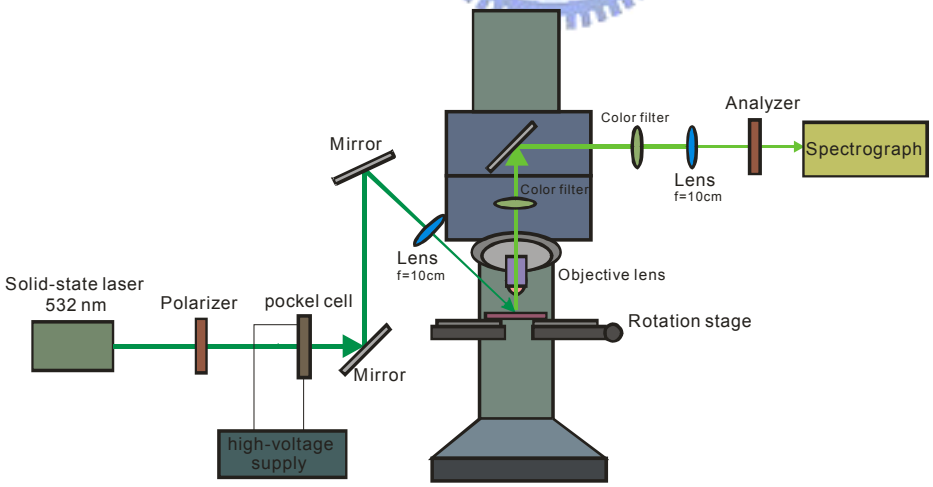

Fig. 3.3: The apparatus used for acquiring polarization-modulating Raman spectrum is shown. The polarization direction of the incident light is controlled with a Pockel cell excited with a sinusoidal wave of half-wave voltage amplitude.

A solid-state CW laser at 532 nm was used as the light source. The polarization

direction of the incident optical field is controlled with a Pockel cell excited with a sinusoidal wave of half-wave voltage. The polarization of the laser beam was first aligned to perpendicular to the incident plane (*i.e.*, the *s*-polarization) without applying HV voltage on the Pockel cell. The laser polarization will be switched to on the incident plane (the *p*-polarization) with a half-wave voltage of approximately 3.35 kV on the pockel cell. The polarization switching is useful to revealing the optical anisotropy of tilted solver nanorods and the distribution of adsorbed molecule on the silver nanorods.

Based on the finding of Ref. [32], which reported the surface enhanced Raman scattering intensity is maximum when the optical incident angle is equal to 45°. we adjusted the incident angle to be closed to 45° accordingly. The substrate under studied was mounted on a rotation stage. We collected the SERS signal by using an objective lens and filtered the optical signal with two Raman filters in order to remove stray photons at 532 nm. Finally, the collected SERS signal was analyzed with a polarizer and was focused onto the entrance slit of a spectrograph.

When the SERS signal was detected with a photon-counting lock-in detection method, a cooled photomultiplier tube (PMT) in a photon-counting mode was used as the photon detector. The applied voltage on the Pockel cell was switched from 0 V to 3.35 kV with a frequency about 1 kHz to switch the polarization of the optical excitation beam from *s*- to *p*-polarization alternatively. By taking the driving signal as the reference of lock-in detection electronics, the image of amplitude and phase of SERS intensity can be obtained.

3.4 Results and Discussion

To characterize the samples prepared for the study, we first deposited a

monolayer of 8CB molecules on an Ag nanorods coated substrate and acquired the Raman spectrum of 8CB molecules.

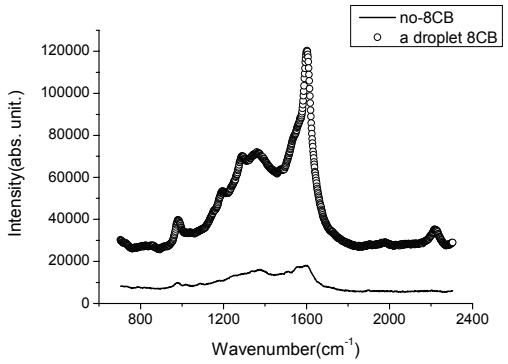

Fig. 3.4: The Raman spectrum of a monolayer of 8CB molecules on an Ag nanordos-coated substrate (red solid line) is presented and the black solid line represents the Raman spectrum of bare substrate coated with tilted Ag nanorods without 8CB molecules.

In Fig. 3.4, the Raman spectrum of the Ag nanorods coated substrate before 8CB molecules were adsorbed is presented in a black-color solid curve. When 8CB molecules were deposited on the substrate, the SERS spectrum becomes much more intense than the bare substrate without 8CB I shown in the red-color solid line.

We first studied the Mie scattering intensity from Ag nanorods coated substrate in order to retrieve the information about the polarizability tensor of Ag nanorod. To achieve the purpose, we define the tilt plane of a nanorod to be composed of the major axis of the nanorod and the substrate normal. The incident plane is composed of the incident excitation beam and the substrate normal. The azimuthal angle is defined to be zero when tilt plane is parallel to the incident plane. When the polarization of the incident beam or the scattering light is perpendicular to the incident plane, it is denoted to be *s*-polarized. Similarly, *p*-polarized field is defined when the polarization of the incident optical field or the scattering field is parallel to the incident plane.

Based on the result of Ref. [13], the major axis of Ag nanorod was found to tilt from the substrate normal by about 73°. We chose the incident angle of the excitation beam to be 45°. With the experimental configuration, the azimuthal pattern of Mie scattering intensity from the Ag nanorods coated substrate was measured and shown in Fig. 3.5. For comparison, the fitting curve to Eq. (3.5) was also presented.

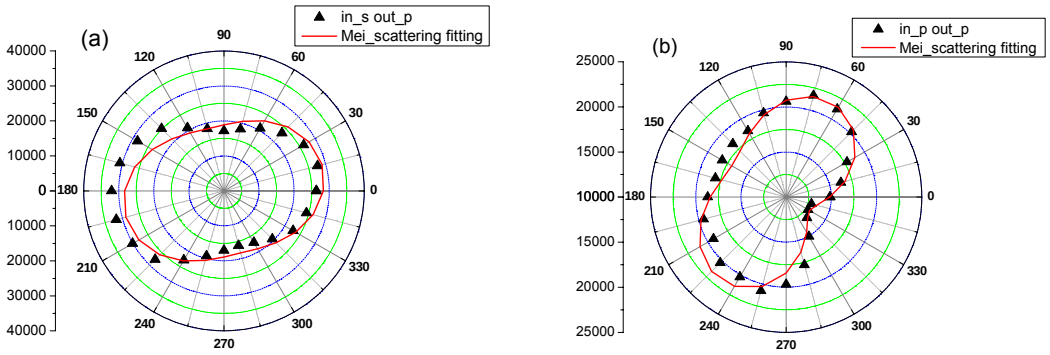

Fig. 3.5: The azimuthal pattern of the Mie scattering intensity from Ag nanorods coated substrate was measured and shown in filled triangles and the fitting curve to Eq. (3.5) (red solid line) is also included for comparison. (a) The incident excitation beam is *s*-polarized while the Mie scattering signal is *p*-polarized. (b) Both of the incident excitation beam and the Mie scattering signal are *p*-polarized.

Comparing Fig. 3.5 (a) to 3.5(b), we found that the azimuthal pattern of the *p*-polarized Mie scattering signal excited with *s*-polarized incident light is more symmetric relative to the incident plane than that excited with *p*-polarized wave. By fitting the two measured *p*-polarized Mie scattering patterns to Eq. (3.5), the polarizability tensor of the tilted silver nanorod can be deduced. The resulting polarizability tensor of the nanorod $\vec{\vec{\alpha}}_r$ was found to be

$$\vec{\vec{\alpha}}_r = \begin{bmatrix} \alpha_{11} & \alpha_{21} & \alpha_{31} \\ \alpha_{21} & \alpha_{11} & \alpha_{31} \\ \alpha_{31} & \alpha_{31} & \alpha_{33} \end{bmatrix} = V \begin{bmatrix} \mathbf{8.17} & \mathbf{0.01} & \mathbf{0.09} \\ \mathbf{0.01} & \mathbf{8.17} & \mathbf{0.09} \\ \mathbf{0.09} & \mathbf{0.09} & \mathbf{4.33} \end{bmatrix}, \qquad (3.13)$$

where V is the volume of nanorod. As expected, the off diagonal components are

much smaller than the diagonal terms. However, it is surprising to find that the x'- and y'-components are larger than that along the z'-axis. This result is contrary to the well known polarizability of the nanorod with nano-scale size that has been obtained by quasi-static appropriation. In Ref. [8], the polarizability can be described by introducing depolarization factors that is associated with aspect ratio for prolate ellipsoidal particle with nano-scale size. And it provides the longitudinal polarizability of prolate ellipsoidal particle is larger than transverse polarizability when quasi-static appropriation is valid. Therefore, we consider the difference of polarizability between quasi-static appropriation and experimental result in this chapter is attributed to the interaction with neighbor nanorods. In general, an isolated prolate ellipsoidal particle is taken into account. But for nanorods array substrate, the distance between nanorods is closed to each other and form bounding of columns along the direction perpendicular to tilt plane of nanorods. It provides the diagonal x'- and y'-components of efficient polarizability of nanorod is larger than that along z'-axis.

For the experimental SERS study of 8CB molecules adsorbed on the Ag nanorods coated substrate, the azimuthal patterns are presented in Fig. 3.6. The azimuthal patterns of SERS are similar to that of bare Ag nanorod coated surbstrate shown in Fig. 3.5, indicating that the adsorbed molecules are most likely orientated along the major axis of the silver nanorod.

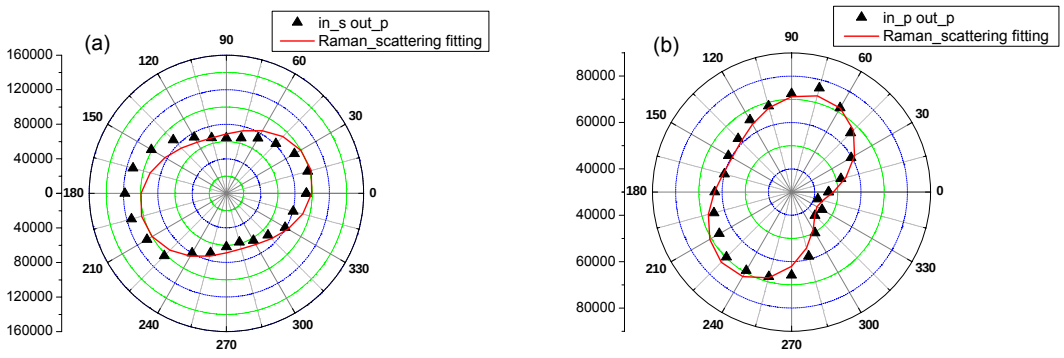

Fig. 3.6: The azimuthal pattern of SERS signal for 8CB molecules adsorbed on a tilted Ag nanorods-coated substrate (triangle) and the fitting curve (red solid line) to Eq. (3.10) and (3.12) are presented. (a) The polarization of incident light used is *s*-polarized and the SERS is *p*-polarized. (b) Both of the incident light and SERS are *p*-polarized.

To further analyze the adsorbed geometry of 8CB molecules on a silver nanorod, we inserted the polarizability of Ag nanorod $\vec{\alpha}_r$, obtained from Mie scattering results of the clean silver nanorod coated substrate, into Eq. (3.10). Combining Eq. (3.10) and Eq. (3.12), the fitting of the azimuthal SERS patterns of specific vibrational peaks of 8CB molecule yields the probability of the adsorbed molecule oriented on nanorod along x' , y' or z'-axis, respectively. The fitting indicates $\rho_{x'}$ is about zero; $\rho_{y'}$ is 6%, and $\rho_{z'}$ is about 94%.

Based on the polarization-resolved SERS results, we can go further to investigate the 2D SERS distribution of specific vibrational modes of 8CB molecule with photo-counting lock-in detection methodology. To do that, we switched the polarization direction of incident light with a Pockel cell at a frequency of 1 kHz. The photon counting stream was processed with a lock-in detection scheme with a reference signal taken from the Pockel cell driving waveform. In Fig. 3.7, the resulting DC, amplitude, and phase components of the modulated SERS signal intensity at 1603 cm^{-1} are presented. The scan area is 1.2×1.2 mm^2.

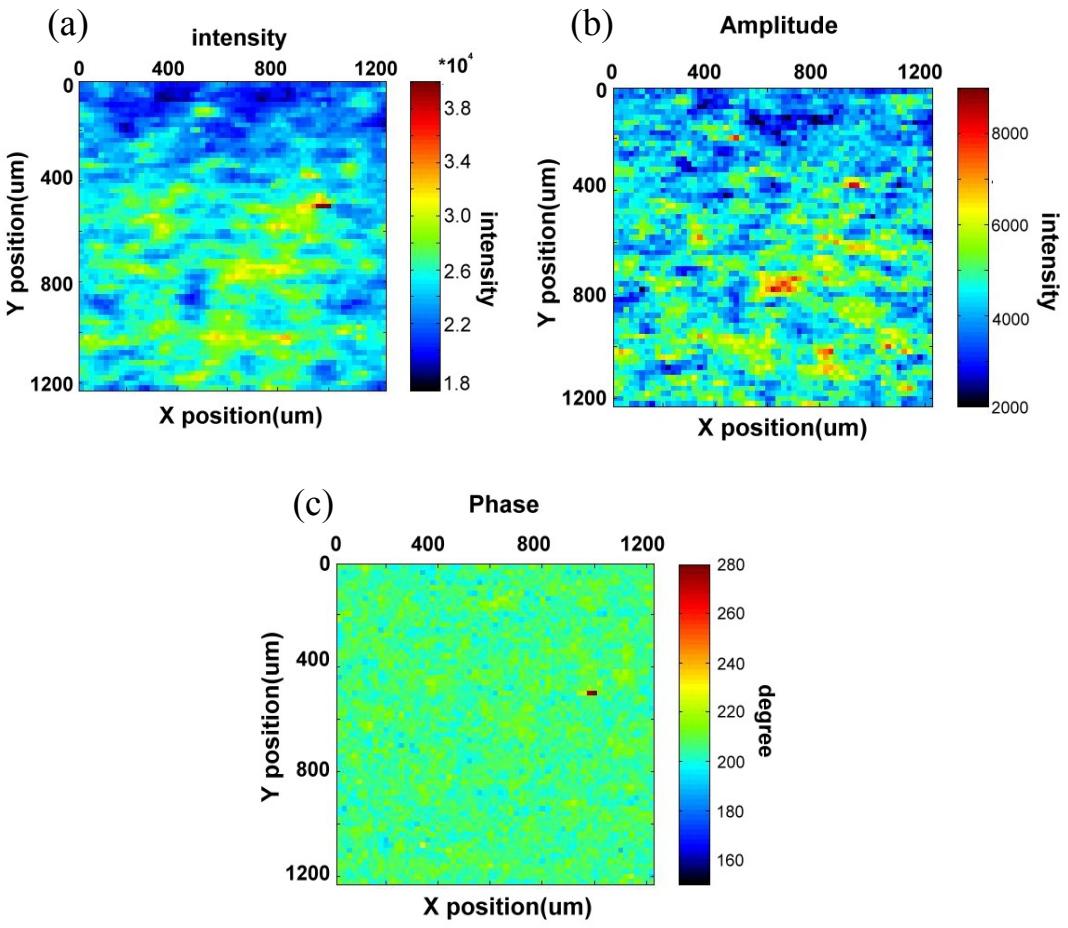

Fig. 3.7: (a) The DC component, (b) the amplitude and (c) the phase image of the modulated SERS signal at 1609 cm^{-1} was acquired by using a photon-counting lock-in detection scheme. The incident light was polarization modulated at a frequency Ω=1 kHz.

Notice that for the computer-based photon-counting lock-in detection scheme depicted in Chapter 2, the measured amplitude component is not equal to the real amplitude of the SERS intensity variation with *s*- and *p*-polarized optical excitation fields. Instead, the real amplitude of the SERS intensity variation is equal to a multiplication of the measured amplitude by $\sqrt{2}$. We can therefore deduce the images of *p*-polarized SERS signal at 1603 cm^{-1} excited with *s*- and *p*-polarized optical field from Fig. 3.7. The resulting images are presented in Fig. 3.8. The phase image of SERS shown in Fig. 3.7 (c) indicates that the SERS intensity is out-of-phase to the reference waveform, indicating that the *p*-polarized SERS intensity excited with

s-polarized field is larger than that obtained with *p*-polarized incident field.

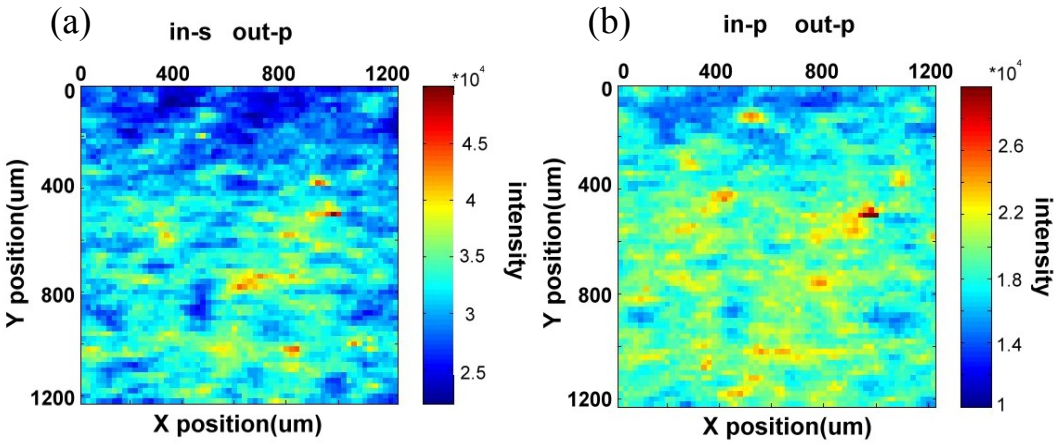

Fig. 3.8: The images of *p*-polarized SERS peak at 1603 cm^{-1} of 8CB molecules adsorbed on a Ag nanorods-coated substrate. The sample was excited with (a) *s*-polarized and (b) *p*-polarized light. The scan area is 1.2×1.2 mm^2.

The variation of the SERS signal shown in Fig. 3.8 is most likely due to the orientation variation of Ag nanorods. The major axis of Ag nanorod projected on the x-y plane can exhibit an azimuthal distribution with a finite distribution width. Considering the measured results of the polarizability tensor of Ag nanorod and the probability of adsorbed 8CB molecules oriented on Ag nanorods, the azimuthal distribution of the major axis of Ag nanorod projected on the x-y plane can be deduced and shown in Fig. 3.9.

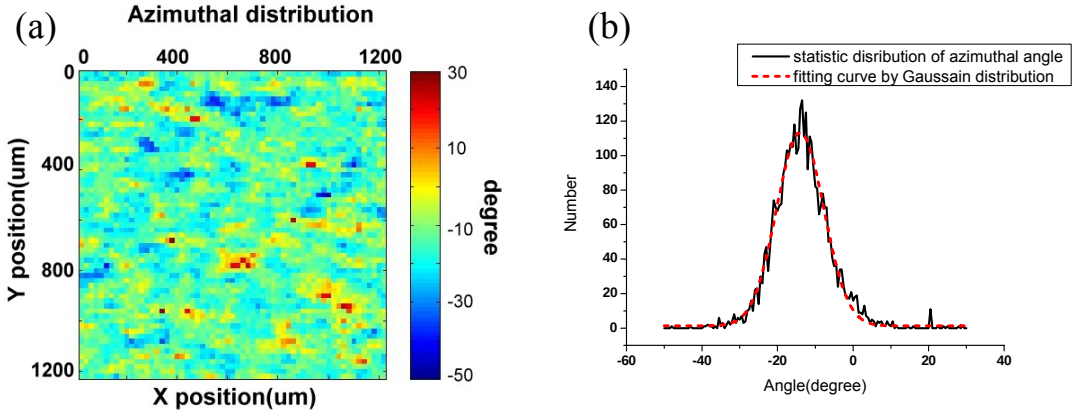

Fig. 3.9: (a) The azimuthal distribution image of the major axis of Ag nanorod projected on the x-y plane is showed. (b) The histogram of the azimuthal distribution image of (a) is shown in the black solid line and the red dashed curve denotes the fit to a Gaussian distribution function.

The azimuthal distribution of the major axis of Ag nanorod projected on the x-y plane in the scanned region (1.2×1.2 mm^2) can be more clearly seen in Fig. 3.9(b). The measured distribution can be fitted to a Gaussian distribution that peaks at -14° and a full width of half maximum (FWHM) is 12.5°.

There is an advantage to determine the azimuthal angle of tilted Ag nanorods on a substrate with photon-counting lock-in detection of SERS intensity of adsorbed molecules. As pointed above, the SERS modulated intensity is out-of-phase to the reference waveform when the Ag nanorods are aligned parallel to the incident plane. The SERS modulated intensity shall become in-phase to the reference waveform when the tilting plane of the Ag nanorods is perpendicular to the incident plane, which was verified and showed in Fig. 3.10. Thus, we can use the phase-sensitive SERS to ambiguously determine whether the tilting plane of the Ag nanorods is parallel or perpendicular to the incident plane.

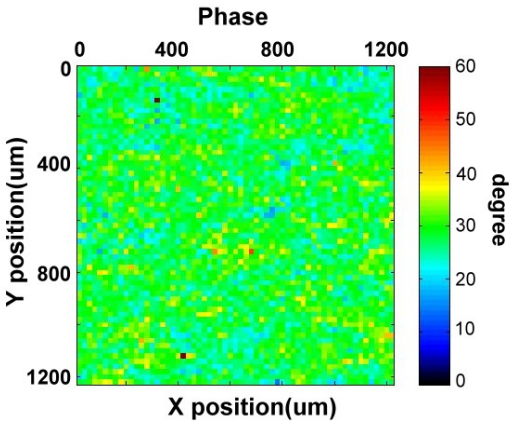

Fig. **3.10**: The phase map of the modulated SERS intensity at 1609 cm^{-1} taken from 8CB monolayer adsorbed on a tilted Ag nanorod-coated substrate. The substrate was

oriented to have the tilting plane of Ag nanorods perpendicular to the incident plane.

Based on the result, we can align that the azimuthal direction of the tilted Ag nanorod to along 0^o or 180^o by comparing the image of *p*-polarized SERS intensity excited with *p*-polarized optical field. For the images of *p*-polarized SERS intensity from tilted Ag nanorods with 0° and 180° azimuthal angle and excited with *s*-polarized incident field are similar as showed in Fig. 3.11. In Fig. 3.11(a), the image taken with the azimuthal angle of Ag nanorod being 0° and the inset inserted at upper right taken with the azimuthal angle to be 180°. When exciting with *p*-polarized optical field, the images of *p*-polarized SERS intensity are different and showed in Fig. 3.11(b). The image taken with the azimuthal angle of Ag nanorod being 0° and the inset inserted at upper right taken with the azimuthal angle to be 180°. We can see that the image of *p*-polarized SERS intensity with 180° of azimuthal angle of Ag nanorod is more intense than that with 0° of azimuthal angle, indicating that the azimuthal angle of Ag nanorod can be distinguish without ambiguity for 0° and 180°. Therefore, the technique with photon-counting lock-in detection to measure phase-sensitive SERS intensity of adsorbed molecules provides unique capability to determine the orientation of tilted Ag nanorods.

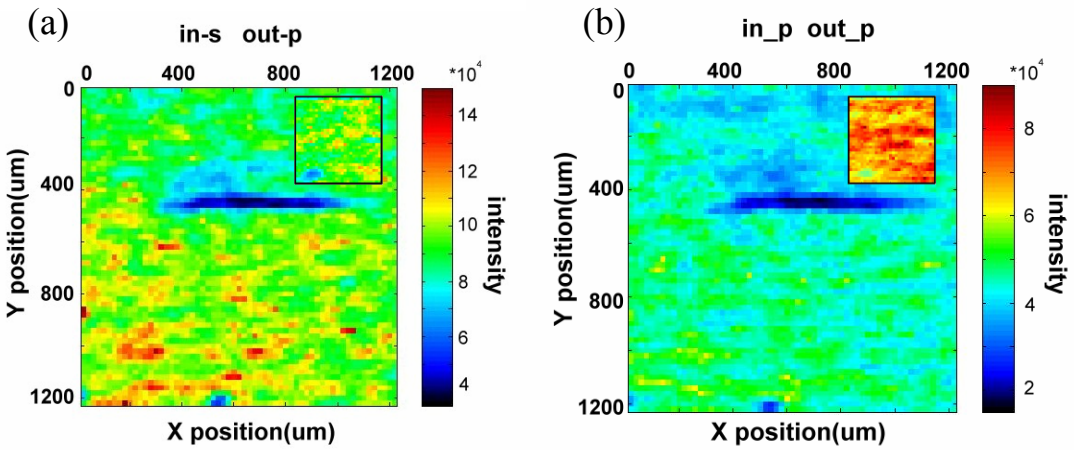

Fig.3.11: The *p*-polarized SERS image in a region of 1.2×1.2 mm^2 of a tilted Ag nanorods-coated substrate. The incident plane was aligned to 0° azimuthal angle of the tilted Ag nanorods and was excited with (a) *s*-polarized light, and (b) *p*-polarized incident light. The inset at the upper right represents that the image of *p*-polarized SERS image taken on a substrate oriented at 180° azimuthal angle of the Ag nanorod.

3.5 Conclusion

In this chapter, a theoretical model of SERS from a monolayer of molecules adsorbed on tilted silver nanorods had been developed. The model allows us to deduce the polarizability tensor of a silver nanorod and the probability of the molecules adsorbed with a specific orientation configuration on tilted Ag nanorods. The photon-counting lock-in detection scheme used to measure phase-sensitive SERS intensity of adsorbed molecules provides unique capability to deduce the orientation of tilted Ag nanorods, which shows the azimuthal distribution of the major axis of Ag nanorod projected on the x-y plane peaks at -14° with a full width of half maximum (FWHM) of 12.5°.

Chapter 4

Probing the Profile of a Focused Gaussian Beam with Scanning Near-Field Optical Microscopy (SNOM)

4.1 Introduction

Advanced in integral optics require some new techniques. In particular, the mapping of optics field propagation in waveguide structure is very important. Scanning near-field optical microscopy is able to provide understanding of these structure devices and optical resolution below the diffraction limit by using a fiber tip. The resolution of SNOM is only limited by the aperture of fiber tip. By raising the technique of manufacture of fiber tip to decrease the aperture of fiber tip, images with higher resolution are acquired and the detected intensity becomes be smaller oppositely. In order to obtain the perfect image with high resolution and intensity simultaneous, a suitable aperture of fiber tip is required. Besides the method that near-field light is collected by a vibrating fiber tip on substrate surface, scattering-type SNOM, that the near-field light is scattered by a probe made of a metal or semiconductor and the scattering light is collected by a confocal-type microscope, is another method and called ASNOM [33]. According to component of interference, SNOM is proposed that there are two kinds SNOM, homodyne and heterodyne SNOM. The homodyne SNOM is that the collected field by a fiber tip is without additional process. And heterodyne SNOM is that additional reference field is provided between interference of collected field and background. The comparison between the two versions of SNOM is presented. However in SNOM or ASNOM,

there is a default that a fiber tip is appropriately closed to the surface of measured device and the distance between fiber tip and surface is only a few nanometers.

4.2 Theory of Heterodyne SNOM

Assuming a fiber tip vibrates vertically above the sample at a frequency *f* (=$\omega_0/2\pi$) with amplitude of several tens nanometers. We define the distribution of electric field above the sample collected by a fiber tip is E_t and the background field E_b originates from scattering occurring at the sample surface. E_b and E_t would be characterized by $E_b = |E_b| e^{i(\omega t+\phi_b)}$ and $E_t = |E_t| e^{i(\omega t+\phi_t)}$, where $(|E_b|, \phi_b)$ and $(|E_t|, \phi_t)$ are the respective amplitude and phase. The schematic is presented below in Fig. 4.1.

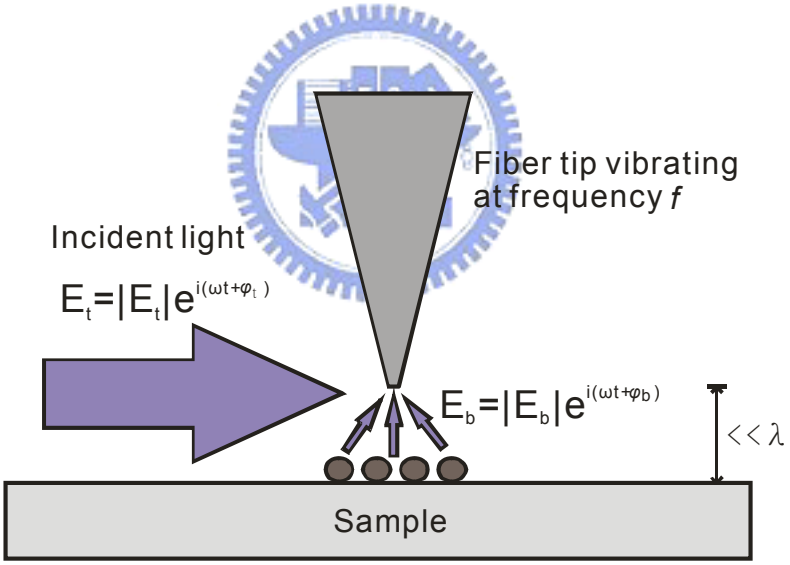

Fig 4.1: The schematic of interference between Et and E_b is presented.

If there are only the two electric fields, E_b and E_t, to interfere each other, the detected intensity I is

$$I = (E_b + E_t) \times (E_b{}^* + E_t{}^*) \tag{4.1}$$

Where E* is the complex conjugate to E. Thus, the intensity

$$
\begin{aligned}
I &= (|E_b|e^{i(\omega t+\phi_b)} + |E_t|e^{i(\omega t+\phi_t)}) \times (|E_b|e^{-i(\omega t+\phi_b)} + |E_t|e^{-i(\omega t+\phi_t)}) \\
&= |E_b|^2 + |E_t|^2 + 2|E_b||E_t|\cos(\phi_t - \phi_b)
\end{aligned} \tag{4.2}
$$

Because the background field is uncontrolled, we raise a controllable field E_r that is frequency shifted by $\triangle\omega$ relative to E_t to replace the background field and the corresponding amplitude and phase are $(|E_r|, \phi_r)$. As a result, the detected intensity I becomes

$$
\begin{aligned}
I &= (E_b + E_t + E_r) \times (E_b{}^* + E_t{}^* + E_r{}^*) \\
&= |E_b|^2 + |E_t|^2 + |E_r|^2 + \\
&\quad 2|E_b||E_t|\cos(\phi_b - \phi_t) + \\
&\quad 2|E_b||E_r|\cos(\triangle\omega t + \phi_r - \phi_b) + \\
&\quad 2|E_t||E_r|\cos(\triangle\omega t + \phi_r - \phi_t) \\
&= I_1 + I_2 + I_3 + I_4 + I_5 + I_6
\end{aligned} \tag{4.3}
$$

There are six terms in Eq. (4.3) for the detected intensity because of interference between three fields. The first three terms (I_1, I_2, I_3) correspond to respective intensities of the three fields. Among the three terms, only $I_2=|E_t|^2$ is varying with time and so that can be extracted by lock-in detection at frequency n*f* (n is an positive integral), filtering $|E_b|$ and $|E_r|$ out. The fourth term is the interference between background field and the distribution of electric field above the sample collected by fiber tip. This term is also modulated by the fiber tip at frequency *f*. Thus, the detected intensity after the lock-in detection at frequency n*f* is

$$
I^f = |E_t|^2 + 2|E_b||E_t|\cos(\phi_b - \phi_t) \tag{4.4}
$$

In general case, the scattering field is much higher for a rough sample and $|E_b|>>|E_t|$, so that the second term dominates in Eq. (4.4). But in less common case, for example to detect a nanoparticle on a smooth surface, $|E_t|^2$ can dominates in Eq. (4.4).

The fifth term I_5, that results from the interference between the background field and the reference field, in Eq. (4.3) can be extracted by lock-in detection at frequency

$\triangle\omega/2\pi$. But this term is not related to the distribution of electric field above the sample, so that it is only used to adjust the interferometer alignment.

Finally, the sixth term I_6 in Eq. (4.3) is interesting and results from interference between the reference field and the distribution of electric field above the sample collected by the fiber tip. Because $|E_t|$ is modulated by the fiber tip at frequency f, the sixth term can be extracted by lock-in detection at frequency nf-$\triangle\omega/2\pi$. The amplitude channel of the lock-in amplifier provides only the amplitude information, independent of background field, on the sample by lock-in detection at frequency nf-$\triangle\omega/2\pi$. And the amplitude can be enhanced by the factor of $|E_r|$ that is controllable. Besides, the phase channel of the lock-in amplifier provides the phase information of electric field on the sample that is related to the phase of reference field. Such information is valuable for investigating the optical physics of numerous devices.

4.3 Experimental Apparatus of SNOM

The laser used for scanning near-field optical microscopy (SNOM) is a solid state laser with pigtail output and a superluminscent light emitting diode. Here the solid state laser is used to be alignment light. The schematic of experimental setup is showed in Fig. 4.2.

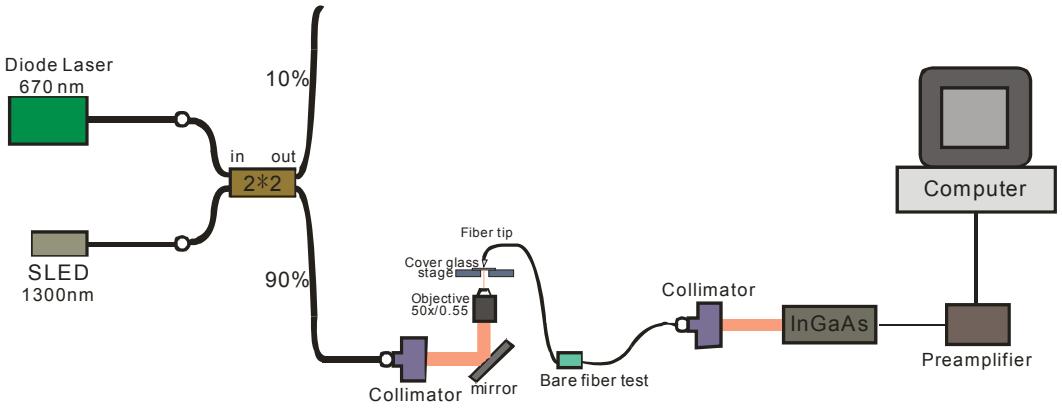

Fig. 4.2: schematic of experimental setup for SNOM

The SLED with wavelength at 1300nm and solid state laser with wavelength at 670nm deliver into a 2×2 coupler for which one output is 10% of total intensity and the other is 90%. We take the 90% output to collimate by using a coupler. The collimated light propagates in free space and then focus on a cover glass by the objective lens, in which the N.A. is 0.55 and magnification is 50X. We collect the intensity of SLED on the cover glass by using a fiber tip which diameter of aperture is about one hundred nanometer and oscillates at a frequency closed to $\omega_0/2\pi$~36 kHz along the z direction. Because the aperture of fiber tip is much small, the collected signal is slight fairly. The collected light propagates through fiber and is collimated by using a collimator. We use the InGaAs detector to measure the intensity of collected light. Thus, the intensity distribution of laser beam focused on the cover glass will be acquired with accuracy about one hundred nanometer through amplifying the detected signal of InGaAs detector.

Heterodyne SNOM will be used to measure the amplitude and phase distribution of spot size focused on cover glass. The schematic setup of heterodyne SNOM be achieved next is represented in Fig. 4.3. [34, 35]

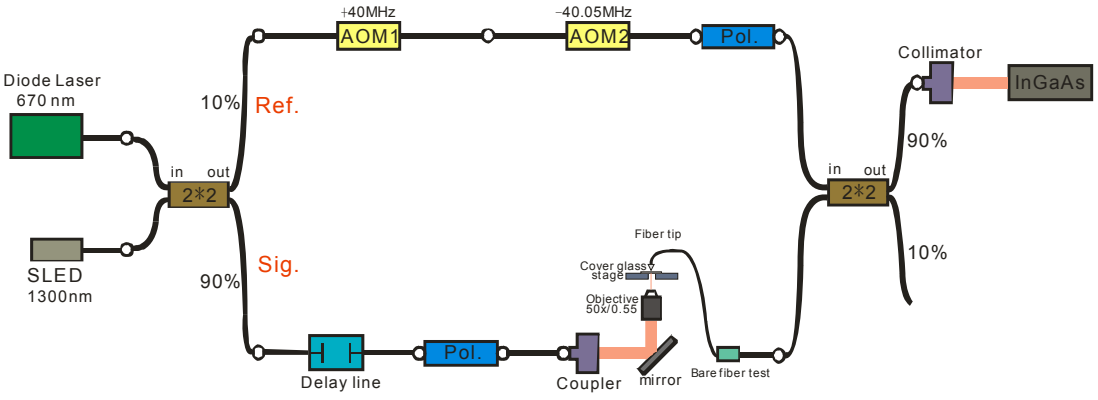

Fig. 4.3: The schematic of experimental setup for heterodyne SNOM

The SLED source is divided into two components, one is 10% and the other is 90% of total intensity. Among this two parts, we define the 90% output of total intensity is

signal path and the 10% output is reference path. For the reference path, oscillation frequency ω of the initial electric field will up-shift 40MHz by one acousto-optic modulator (AOM) and down-shift 40.05MHz by the other AOM, so oscillation frequency of the final electric field through this two AOM is ω+△ω where △ω~-50 kHz. Besides, we place the polarization controller to operate the polarization of the light inside single mode fiber and input to 2×2 coupler finally. For the signal path, there is the delay line which resolution is about 0.05 mm (0.33 ps) and total available range is 18 cm (600 ps) to adjust the length of signal path to match the length of reference path. Only when the difference of length of signal path and reference path is smaller than the coherent length of light source, the two path of light will interfere with each other. At this path, we also place one polarization controller to control the polarization. Then the light inside single mode fiber is collimated nearly by a coupler and focused on cover glass by the objective lens. The light intensity on cover glass will be collected through the fiber tip with rapidly oscillation (about 36 kHz) along the z direction and finally propagates to 2×2 coupler. Thus, there will be interfere phenomenon at the 2×2 coupler and detected by the InGaAs. In order to extract the amplitude and phase distribution on cover glass, the signal is demodulated by a Lock-in amplifier.

4.4 The Experimental Results by Using SNOM Technology and Conclusion

We adjust the propagation of SLED beam through center of back aperture of the objective lens and to be orthogonal with surface of cover glass. Besides, the initial location of fiber tip needs to be adjusted around the focused spot on the cover glass when approaching the fiber tip to cover glass. Here we define the beam propagate

along z direction and the height of objective lens is the origin of z direction when the cover glass locates near focus plane. We measured the distribution of optical intensity on the cover glass by amplifying the signal that is detected by InGaAs detector about sixty times when the cover glass locates near focus plane. It shows the result of twice continuous measurements in Fig. 4.4.

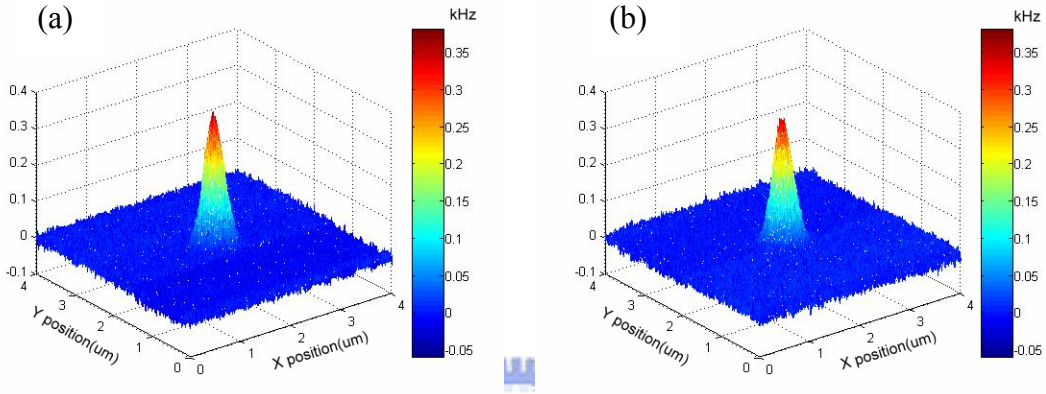

Fig. 4.4: The distribution of optical intensity on a cover glass is collected by the fiber tip. When the focus plane of the SLED at wavelength 1.3 μm focused by the objective lens (0.55/50X) is on a cover glass, the results of twice continuous measurements is showed respectively at (a) and (b) in SNOM experiment.

The scale of z direction is kHz in Fig. 4.4 and can switch to Volt by using 1 V=2 kHz. By fitting the distribution of optical intensity, we acquire respectively that the spot size of (a) is 0.2 μm and (b) is 0.205 μm. From the result showed in Fig.4.4, we make sure this experiment is repeatable. According to the diffraction limit, the minimum spot size is $w_0 = 0.61 \times \frac{\lambda}{N.A.} \sim 1.442$ (μm), λ is the wavelength of incident light and N.A. is numerical aperture of objective lens, at focus plane. But the experimental spot size is much smaller than theoretical spot size obviously. The reason is that the optical intensity detected by InGaAs is too slight to distinguish the outer intensity of spot size even through amplifying the signal about sixty times. We can find that the maximum intensity on cover glass is only 0.185 mV. As a result, the spot size measured in this

experiment is not the real spot size at focus plan completely.

In order to understand the characteristic of beam profile focused by objective lens, we adjust the position of objective lens in z direction to shift up or down away from origin of z direction. It shows respectively the distribution of optical intensity on cover glass in Fig. 4.5 when the objective lens is shifted (a) down or (b) up away from origin of z direction about 15 μm approximately.

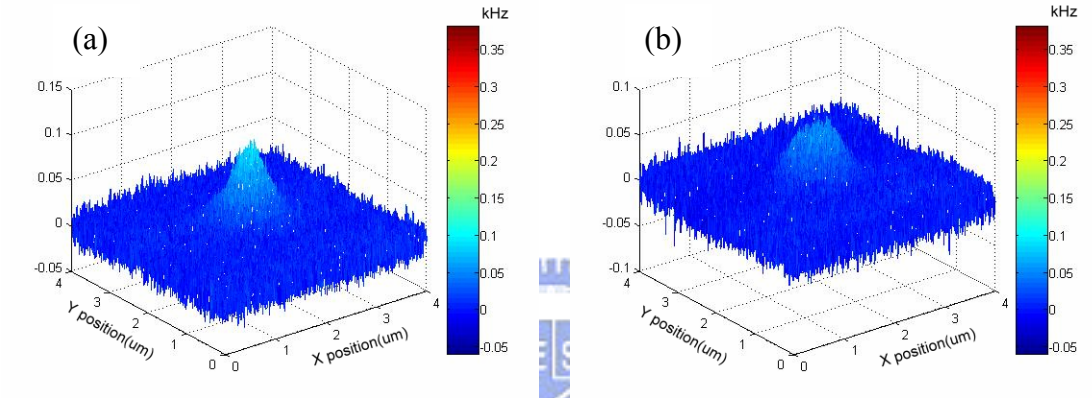

Fig. 4.5: When the focus plane of the SLED at wavelength 1.3 μm focused by the objective lens (0.55/50X) is at approximately 15 μm (a) below or (b) above the cover glass, the distribution of optical intensity collected by the fiber tip on the cover glass is presented respectively.

By fitting the distribution of optical intensity on cover glass respectively in Fig. 4.5, we acquire the spot size is 0.405 μm when the objective lens shifts 15 μm down away from origin of z direction and the spot size is 0.445 μm when the objective lens shifts 15 μm up away from origin of z direction. It provides the information that the distance between focus plane and cover glass is not equal completely for shifting the objective lens up and down 15 μm away from the origin of z direction. The condition that experimental spot size is smaller than the theoretic minimum spot size is also presented here and the reason is mentioned above.

Table 4-1 The corresponding spot size for different position of the objective lens in z direction in SNOM experiment.

Position of the objective lens in z direction.	The spot size on cover glass acquired by fitting the experimental data of SNOM
+15 μm	0.445 μm
+5 μm	0.21 μm
0	0.2 μm
-5 μm	0.24 μm
-15 μm	0.205 μm

Besides shifting the objective lens up or down 15 μm away from origin of z direction, we also take measurement of the distribution of optical intensity on cover glass for shifting the objective lens up or down 5 μm away from origin of z direction. The corresponding spot size respectively for shifting the objective lens up or down 5 μm away from origin of z direction is 0.21 μm and 0.24 μm. We frame a table showed in Table. 4-1 for the spot size related to the position of objective lens in z direction. According to the position of objective lens in z direction and corresponding spot size in this experiment, it represents the schematic of beam profile focused by the objective lens in Fig. 4.6.

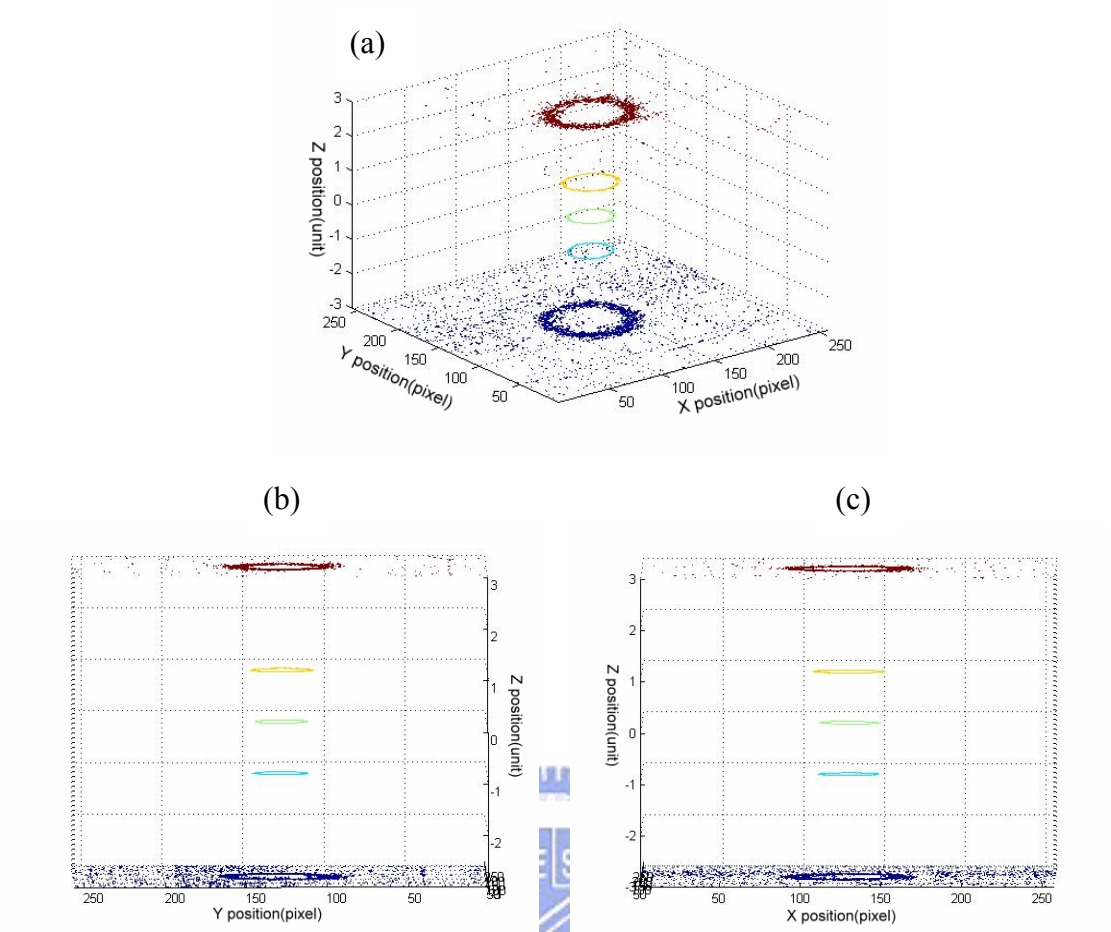

Fig. 4.6 (a) Schematic for spot sizes of beam profile focused by the objective lens along z direction at different z position. (b) and (c) present the view of x direction and y direction of (a), respectively.

The scale of z direction means that 1 unit is equal to 5 μm in Fig. 4.6. According to theoretical calculation, the depth of focus of objective lens is $\pm d \sim \frac{\lambda}{(N.A)^2}$ =4.3 (μm) and it means the spot size varies slowly inside the depth of focus for a Gaussian beam. As a result, the middle three spot sizes near origin of z position are almost the same size, and the outer two spot sizes far away from origin of z position become larger obviously among the spot sizes of focused beam profile in SNOM experiment. We can find that the depth of focus experimentally in Fig.4.6 is closed to the theoretical depth of focus for a focused Gaussian beam.

In order to overcome that the distribution of real spot size of beam profile can

not be acquired completely in SNOM experiment, we will investigate the distribution of electric field for a focused Gaussian beam by using heterodyne technology further. When we take heterodyne SNOM to measure the distribution of amplitude and phase of electric field on cover glass, there is the amplitude of reference field |Er| multiplying the amplitude of electric field collected by the fiber tip $|E_t|$ in six term of Eq.4.3 to enhance the intensity. Because the amplitude of reference field |Er| is much stronger than $|E_t|$, the efficiency of enhancement by the amplitude of reference field in heterodyne SNOM is better than by the preamplifier in SNOM experiment. Thus, the distribution of amplitude and phase of electric field on cover glass can be distinguished completely.

As a result, although we can not acquire the real spot size of beam profile for a focused Gaussian beam by using SNOM technology, the tendency of beam profile of a focused Gaussian beam is provided and the resolution of spot size can be achieved to one hundred nanometers below the diffraction limit. Next, the distribution of amplitude and phase of electric field on cover glass will be respectively acquired by using heterodyne SNOM technology. Further, the propagating information of electric field inside numerous devices will be also obtained and optical resolution is below the diffraction limit by using heterodyne SNOM technology.

Chapter 5

Conclusions and Future Prospect of This Thesis Study

In conclusion of this thesis, we demonstrate that photon counting lock-in detected Raman imaging technique not only effectively suppresses the nonresonant background of Raman spectrum, but also yields the information about the modulation amplitude and phase of specific Raman peak. And the reduction factor from the phase relaxation time to the amplitude relaxation time is useful to reflect the disordering effect of the FLC alignment from the high-frequency driving. It provides the field-induced reorientation dynamics of the nc-ZnO doped SSFLC film is generally more organized and therefore less sensitive to the high frequency driving induced disordering. The result is also supported by the CV characterization.

For surface enhanced Raman scattering section, stimulated Raman scattering intensity of monolayer molecule on Ag nanorods array substrate is indeed enhanced more order of magnitude intense than transition Raman scattering intensity. Due to high aspect ratio of nanorod, Mei-scattering and enhanced Raman scattering are dependent on azimuthal angle of nanorod. The polarizability tensor of Ag nanorod is obtained by Mei-scattering and probability of orientation of adsorbed molecule on Ag nanorods array is provided by combining Mie scattering and Raman scattering. Besides, the phase-sensitivity Raman image of monolayer molecule on nanorods array substrate is obtained and analyzed by using computer-based photon-counting lock-in detection. It provides a simple technique to determine the orientation of nanorods array and the statistic distribution of azimuthal angle. In SNOM section, although we can not obtain the real spot size of beam profile by using SNOM technology, the

tendency of beam profile of a focused Gaussian beam is provided and the resolution of spot size can be achieved to one hundred nanometers below the diffraction limit.

In the future, we will be able to take advantage of these technologies to investigate dynamic behavior of some devices and break through some limit of optical microscopy, such as slight optical signal and amplitude and phase distribution of nanoscale structure below diffraction limit by accomplishing heterodyne SNOM.

References

[1] T. Vo-Dinh, "Surface-enhanced Raman spectroscopy using metallic nano-structure, " *Trends Analyt. Chem.*, **17**, 557 (1998).

[2] C.R. Yonzon, D.A. Stuart, X. Zhang, A.D.McFarland, C.L.Haynes and R. P.Van Duyne, "Towards advanced chemical and biological nanosensors-An overview," *Talanta*, **67**, 438 (2005)

[3] P. C. Andersen and K. L. Rowlen, *Appl. Spectrosc.*, **56** 124A (2002)

[4] P. N. Bartlett, J. J. Baumberg, S. Coyle, and M. E. Abdelsalam, *Faraday Discuss.* **125**, 117 (2004)

[5] U. Kreibig and M. Vollmer, "*Optical properties of metal clusters*," Springer-Verlag, Berlin, 1995.

[6] L. A. Sweatlock, S. A. Maier, H. A. Atwater, J. J. Penninkhof and A. Polman, *Phys. Rev. B*, 71, 235408 (2005)

[7] A. Bouchelier, R. Bachelot, J. S. Im, G. P. Wiederrecht, G. Lerondel, S. Kostcheev and P. Royer, *J. Phys. Chem. B*, **109**, 3195 (2005)

[8] E. Stefan Kooij and Bene Poelsema, *Phys. Chem. Chem. Phys.*, 8, 3349 (2006)

[9] A. A. Stacy and R. P. Van Duyne, *Chem. Phys. Lett.*, **102**, 365 (1983)

[10] K. T. Carron, X. Gi, M. L. Lewis, *Langmuir*, **7**, 2-4 (1991)

[11] T. R. Jensen, M. D. Malinsky, C. L. Haynes and R. P. Van Duyne, *J. Phys. Chem. B*, **104**, 10549 (2000)

[12] G. Suer, U. Nickel and S. Schneider, *J. Raman Spectrosc*., **31**, 359 (2000)

[13] Y.-P. Zhao, Stephen B. Chaney, Saratchandra Shanmukh, and Richard A. Dluhy**,** *J. Phys. Chem. B*, 110, 3153 (2006)

[14] Leon Abelmann and Cock Lodder, "Oblique evaporation and surface diffusion", *Thin Solid Films*, **305**, 1-21 (1997)

[15] Dieter Braun and Albert Libchaber, "Computer-base photon-counting lock-in for phase detection at the shot-noise limit," *Opt. Lett.*, **27**, 1418-1420 (2002).

[16] N. A. Clark, S. T. Lagerwall, *Appl. Phys. Lett.*, **36**, 899 (1980).

[17] S. T. Lagerwall, *Ferroelectric and Antiferroelectric Liquid Crystals* (Wiley-VCH, Weinheim, 1999).

[18] Felix 017/100 FLC mixture, commercial room-temperature FLC mixture by Clariant (Frankfurt, Germany) Cr -28°C SmC* 73°C SmA* 77°C N* 85°C iso (data provided by Clariant).

[19] E. A. Meulenkamp, *J. Phys. Chem. B*, **102**, 5566 (1998).

[20] J. Y. Huang, and W. T. Shih, *J. Phys. C*, **18**, 7593 (2006).

[21] Jung Y. Huang, Liu S. Li, and Ming C. Chen: "Doping with ZnO Nanocrystals Improves Application Properties of Surface-Stabilized Ferroelectric Liquid Crystal," *Phys. Rev. E* (2006), submitted.

[22] S. L. Miller, J. R. Schwank, R. D. Nasby, M. S. Rodgers, *J. Appl. Phys.*, **70**, 2849 (1991).

[23] M. Rahman, S. K. Kundu, B. K. Chaudhuri, *J. Appl. Phys.*, **98**, 024114 (2005).

[24] C. Reynaerts, A. De Vos, *J. Phys. D*, **22**, 1504 (1989).

[25] P. Yang, D. L. Carroll, J. Ballato, R. W. Schwartz, *Appl. Phys. Lett.*, **81**, 4583 (2002).

[26] W. T. Shih, J. Y. Huang, and J. Y. Zhang, *Liq. Cryst.*, **31**, 377 (2004).

[27] D.-S. Wang and M. Kerker, *Phys. Rev. B*, **24**, 1777 (1981)

[28] Joel Gersten and Abraham Nitzan, *J. Chem. Phys.*, **73**, 3023 (1980)

[29] S. B. Chaney, Z. -Y. Zhang, and Y. -P. Zhao, *Appl. Phys. Lett.*, **89**, 053117-1 (2006)

[30] Leon Abelmann and Cock Lodder, *Thin Solid Films*, **305**, 1-21 (1997)

[31] S. B. Chaney, S. Shanmukh, R. A. Duluhy, and Y.-P. Zhao, *Appl. Phys. Lett.*, **87**, 031908 (2005).

[32] Yongjun Liu, Jianguo Fan, and Y.-P. Zhao[a)], Saratchandra Shanmukh and Richard A. Dluhy, *Appl. Phys. Lett.*, **89**, 173134 (2006)

[33] Lewis Gomez, Renaud Bachelot, Alexandre Bouhelier, Gary P. Wiederrecht, Shih-hui Chang, Stephen K. Gray, Gilles Lerondel, Feng Hua, Seokwoo Jeon, John A. Roger, Miguel E. Castro, Sylvain Blaize, Ilan Stefanon and Pascal Royer, *Apertureless Scanning Near-field Optical Microscopy: a comparison between homodyne and heterodyne approaches.*

[34] A. Nesci and Y. Fainman, "Complex amplitude of an ultra-short pulse with femtosecond resolution in a waveguide using a coherent NSOM at 1550 nm", 48th SPIE Annual Meeting Symposium, SPIE Proc. to be published, San Diego, USA, 2003.

[35] Ilan Stefanon, Sylvain Blaize, Aurélien Bruyant, Sébastien Aubert, Gilles Lerondel, Renaud Bachelot, and Pascal Royer, *Optical Express*, **13**, 5553 (2005)